

Blockage of saline intrusions in restricted, two-layer exchange flows across a submerged sill obstruction

Alan Cuthbertson¹ · Janek Laanearu² · Magda Carr³ ·
Joel Sommeria⁴ · Samuel Viboud⁴

Received: 31 May 2016 / Accepted: 9 March 2017 / Published online: 23 March 2017
© The Author(s) 2017. This article is an open access publication

Abstract Results are presented from a series of large-scale experiments investigating the internal and near-bed dynamics of bi-directional stratified flows with a net-barotropic component across a submerged, trapezoidal, sill obstruction. High-resolution velocity and density profiles are obtained in the vicinity of the obstruction to observe internal-flow dynamics under a range of parametric forcing conditions (i.e. variable saline and fresh water volume fluxes; density differences; sill obstruction submergence depths). Detailed synoptic velocity fields are measured across the sill crest using 2D particle image velocimetry, while the density structure of the two-layer exchange flows is measured using micro-conductivity probes at several sill locations. These measurements are designed to aid qualitative and quantitative interpretation of the internal-flow processes associated with the lower saline intrusion layer blockage conditions, and indicate that the primary mechanism

Electronic supplementary material The online version of this article (doi:[10.1007/s10652-017-9523-2](https://doi.org/10.1007/s10652-017-9523-2)) contains supplementary material, which is available to authorized users.

✉ Alan Cuthbertson
a.cuthbertson@hw.ac.uk

Janek Laanearu
janek.laanearu@ttu.ee

Magda Carr
magda.carr@st-and.ac.uk

Joel Sommeria
joel.sommeria@legi.cnrs.fr

Samuel Viboud
samuel.viboud@legi.cnrs.fr

¹ School of Energy, Geoscience, Infrastructure and Society, Heriot Watt University, Edinburgh, UK

² School of Engineering, Tallinn University of Technology, Tallinn, Estonia

³ School of Mathematics and Statistics, University of St Andrews, St Andrews, UK

⁴ Laboratoire des Écoulements Géophysiques et Industriels (LEGI), University of Grenoble, Grenoble, France

for this blockage is mass exchange from the saline intrusion layer due to significant interfacial mixing and entrainment under dominant, net-barotropic, flow conditions in the upper freshwater layer. This interfacial mixing is quantified by considering both the isopycnal separation of vertically-sorted density profiles across the sill, as well as calculation of corresponding Thorpe overturning length scales. Analysis of the synoptic velocity fields and density profiles also indicates that the net exchange flow conditions remain subcritical ($G < 1$) across the sill for all parametric conditions tested. An analytical two-layer exchange flow model is then developed to include frictional and entrainment effects, both of which are needed to account for turbulent stresses and saline entrainment into the upper freshwater layer. The experimental results are used to validate two key model parameters: (1) the internal-flow head loss associated with boundary friction and interfacial shear; and (2) the mass exchange from the lower saline layer into the upper fresh layer due to entrainment.

Keywords Exchange flows · Net-barotropic flows · Saline intrusion blockage · Sill obstructions · Stratified flow · Mixing and entrainment · Internal-flow hydraulic modelling

1 Introduction

The presence of natural topographic flow obstructions (e.g. sills, sand bars) can have significant implications for the intrusion of saline marine waters into semi-enclosed estuarine impoundments or fjordic basins. For example, the obstruction of exchange flows within partially-blocked estuaries can impact adversely on estuarine ecology due to the inhibition of tidal intrusion across submerged sand bars at the river mouth, with the suppression of associated estuarine circulation and mixing processes exacerbating stagnation and contaminant accumulation problems within the estuarine impoundments [2, 3]. There are a number of field observations in the semi-closed seas such as the Baltic Sea [12–14, 16, 18], which indicate that two-way patterns of internal flow are present under different background vorticity conditions, associated with extensive mixing near permanent fronts [19]. In coastal regions, some estuaries can be completely blocked from saline marine water intrusion into the river basin, while others are strongly influenced by saline water circulations in the estuary mouth, with restricted intrusion into the estuary basin flowing in the opposite direction to the overlying freshwater outflow layer [22]. Such bi-directional stratified flows can lead to significant depthwise variations and strong gradients in both velocity and density profiles, leading to high gradient Richardson numbers [17, 22]. The dynamics of these exchange flows can be represented by the position of two interfaces, namely (i) the density interface separating the intruding saline water from the overlying, outflowing fresh water layer and (ii) the zero-velocity interface determined by the reversal point in the velocity profile. Turbulent fluxes within the strong interfacial shear layer generated can result in significant interfacial mixing and transfer of mass and momentum between the layers. In some cases, strong vertical entrainment is present within the region of the salt-water return flow, while, in other circumstances, interfacial waves are first formed at the density interface; the interfacial instabilities (e.g. Kelvin–Helmholtz or Holmboe instabilities) providing an additional mechanism for vertical mixing across the density interface.

The study of Farmer and Armi [5] concentrated on investigating the initial dynamics of stratified flows developing over submerged topography. Comparing their observations with numerical simulations [6], they found that, although the model agreed moderately well with the observed end state, it failed to reproduce the observations during the period of flow establishment. They concluded that the bottom boundary dynamics had a fundamental role in the initial evolution of the flow and that numerical models which aim to simulate stratified flows in a sill region must accurately represent the bottom boundary layer. More recently, Negretti et al. [20] and Fouli and Zhu [7] conducted experiments to investigate the mechanisms by which interfacial waves are generated in two layer exchange flows over submerged bottom sills, focusing on the influence of barotropic forcing and the generation conditions for Kelvin–Helmholtz instabilities, respectively. Negretti et al. [21] also investigated the influence of boundary roughness on the generation and collapse mechanisms for large scale interfacial waves in two layer flows down a slope, defining two main sources of entrainment associated with the waves themselves and the bottom roughness. Despite these investigations, there have been relatively few detailed laboratory investigations of the effect of bottom boundary dynamics on sill exchange flows to date. Furthermore, as these near bed processes are expected to induce suspension and transportation of bed sediments, they are, thus, important for mass transport and water quality within coastal regions of restricted exchange [9, 10].

In restricted bi-directional stratified flow problems, the internal flow dynamics are expected to be sensitive to (i) the dimensions of the obstruction (i.e. sill length, height and submergence depth), (ii) density (and stratification) differences between the two water bodies separated by the sill obstruction and (iii) external barotropic forcing conditions due to tidal and freshwater inflows [7, 20]. In this context, however, the range of parametric conditions under which these restricted exchange flows are initiated (or indeed blocked) are not, as yet, completely understood. In addition, further research is required to investigate the physical mechanisms associated with shear-induced mixing processes, vertical entrainment and the generation of interfacial waves by bi-directional flows across the obstruction. Improved knowledge of the bottom boundary dynamics associated with the intrusion of marine saline waters is also required to parameterise boundary layer processes associated with restricted, bi-directional stratified flows across topographic obstructions. These processes, in particular, are known to be crucial for water circulation, mixing, stratification, deep-water renewal, bottom stagnation and flushing within these semi-enclosed water bodies, although their exact role in each of these processes remains somewhat unclear.

Internal hydraulic theory can provide a useful analytical modelling approach for the preliminary interpretation of the complicated internal flow dynamics of restricted, two-layer exchange flows across a submerged sill obstruction. In this regard, Zhu and Lawrence [24] included frictional and non-hydrostatic effects in their two-layer hydraulic model to investigate the case of a baroclinic exchange flow within a silled channel connecting two homogeneous water reservoirs of different densities. It was found from their study that the interface elevations measured at different sections, both in the vicinity of the sill obstruction and at more remote channel locations, corresponded well to predicted elevations from internal hydraulic theory when the internal flow head loss was specified in the range 0.0–0.1 of the total fluid depth. Cuthbertson et al. [2, 3] applied successfully a similar two-layer exchange flow model to consider the case of a slowly descending barrier, initially separating two water reservoirs of different density. Within their investigations, the rate of descent of the barrier was assumed (correctly) to be sufficiently slow for the unsteady two-layer exchange flow generated above the sill crest to adjust continuously to

the appropriate quasi-steady conditions at every stage of the barrier descent. Their results demonstrated that the thicknesses of the two layers at the barrier crest could be predicted satisfactorily by an internal hydraulic model that (i) assumed the existence of either one single control point (i.e. at the barrier crest—[3] or at two control points (i.e. at the barrier crest and channel exit—[2]; and (ii) incorporated internal flow losses from the sudden expansion and contraction of the upper and lower layers, respectively, at the channel exit [3]. In the present study, these two-layer exchange flow models for rectangular-shaped channels have been extended to include both frictional and entrainment effects, which are required to account for turbulent stresses and mass transfer from the lower saline layer (i.e. due to entrainment). As such, the experimental results are used to validate two key parameters in the internal flow model, namely: (i) the flow rate ratio q^* of upper fresh and lower saline layers; and (ii) the mass exchange m from the lower saline layer into the upper fresh water layer. The theoretical results will thus be compared directly with the experimental findings. In this context, a key aim of the current study is to (i) address current knowledge gaps on interfacial mixing processes in bi-directional stratified flows generated across a submerged obstruction, and (ii) define the parametric influences (i.e. flow, density difference and obstruction submergence depth) on shear-driven mixing and entrainment dynamics across the sill, as well as the physical mechanisms associated with blockage of saline intrusions.

2 The physical system

A schematic representation of the physical system under investigation is shown in Fig. 1. A trapezoidal-shaped, submerged sill obstruction S of height h_s , sill length l_s and approach slopes α_s is installed in a rectangular channel of overall length L , width B and depth H . This sill obstruction restricts the exchange flows generated between a freshwater impoundment I and the saline water basin M .

The initial, undisturbed experimental configuration was one in which the rectangular channel is filled with freshwater of density ρ_1 , submerging the trapezoidal sill to a depth h_b ($=H - h_s$). Saline water of density ρ_2 is then introduced at the bottom of basin M at an initially low volume flux Q_2 to allow a dense stratified layer to develop, whilst minimising mixing with the overlying fresh water layer. Once this layer is established, the saline water volume flux Q_2 is increased to a prescribed flow rate and a dense water intrusion is initiated

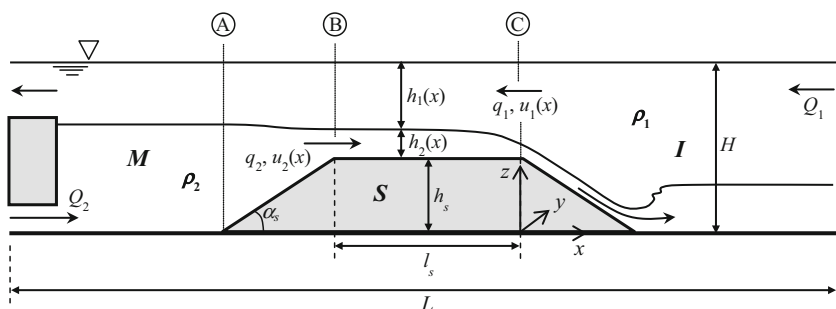


Fig. 1 Schematic representation of physical system under investigation. Sections A, B and C indicate the locations defined in the idealised internal-flow hydraulic modelling approach (see Sect. 4) where internal hydraulic controls are expected to form (i.e. at location A and in the sill region between B and C)

 Springer

above the channel floor, and inclined sill approaches set at an angle $\alpha_s = 26.57^\circ$ (see Fig. 2a). The walls of the rectangular channel were constructed from transparent acrylic to facilitate laser flow illumination and visualization of the bi-directional stratified flow development across the sill. It is noted that the basin-sill slope transitions in the current configuration are expected to have negligible effects on the internal-flow dynamics resulting from flow separation or other non-hydrostatic effects.

With the circular basin and rectangular channel filled with freshwater to a total depth $H = 0.85\text{--}1.0$ m, the counter-flowing saline water ($\rho_1 = 1004.7\text{--}1009.6$ kg m $^{-3}$) and overlying freshwater ($\rho_0 = 1000$ kg m $^{-3}$) layers were externally driven across the submerged sill obstruction. The saline water was delivered to the bottom of basin M via a gravity feed system and 0.3 m-high by 1.5 m-wide rectangular manifold section (Fig. 2a), while fresh water was recirculated within the channel and surrounding circular tank by two centrifugal pumps positioned in the upper part of basin M , directly above the saline water manifold (Fig. 2b). These two flow systems provided saline and fresh water volume fluxes in the ranges $Q_2 = 2.64\text{--}6.94$ l s $^{-1}$ (i.e. $q_2 = Q_2/B = 0.00176\text{--}0.00463$ m 2 s $^{-1}$) and $Q_1 = 0\text{--}30$ l s $^{-1}$ (i.e. $q_1 = Q_1/B = 0\text{--}0.02$ m 2 s $^{-1}$), respectively. In all experimental runs, the saline volume flux Q_2 was held constant while the freshwater volume flux Q_1 was increased systematically in incremental steps (i.e. $Q_1 = 0, 3, 11, 18, 26$ and 30 l s $^{-1}$) at prescribed elapsed times t , with corresponding quasi-steady, exchange flow conditions developing across the sill for each $Q_1:Q_2$ combination. In order to maintain a quasi-constant depth H (and sill submergence depth h_b) within the channel and surrounding basin during each experimental run, water was drained continuously from the bottom of the circular basin, outside the rectangular channel, at a flow rate equivalent to the saline inflow volume flux Q_2 . The parametric dependence of the bi-directional stratified flow conditions developed across the sill obstruction was therefore tested in relation to (i) the relative sill submergence depth $h_b/H = (1 - h_s/H) = 0.5\text{--}0.6$; (ii) the relative density difference of the fresh and salt water inflows, i.e. $(\rho_2 - \rho_1)/\rho_1 = 0.005\text{--}0.01$; and (iii) the relative magnitude of fresh and saline water volume fluxes, i.e. $Q_1/Q_2 (= q_1/q_2) = 0\text{--}11.36$. Summary details of the parametric experimental conditions tested are presented in Table 1. (Note: full details of individual run parameters are given in the supplementary material—Table S1).

3.2 Instrumentation and measurements

Experimental measurements focused mainly on obtaining high resolution density and velocity fields both across the sill obstruction and at selected locations within basins M and I (i.e. on either side of the obstruction) for the range of different bi-directional stratified flows tested. Flow illumination was provided by a continuous laser system sited at the far end of basin I , which produced a vertical laser light sheet aligned along the channel centerline (see Fig. 2a). Two-dimensional Particle Image Velocimetry (PIV) was then used to measure velocity fields within the resulting vertical (XZ) plane, employing two side-mounted digital CCD cameras (Dalsa 1M60, resolution 1024×1024 pixel) to record both instantaneous flow velocity fields at a frame acquisition rate of 10 Hz within specific regions of interest (i.e. across the 2 m-long sill section and on the down-sloping face of the sill obstruction into basin I) (see Fig. 2a). These PIV measurements were obtained over two minute durations for each parametric flow condition tested, allowing synoptic (i.e. time-averaged) velocity fields to be generated for the regions of interest. The PIV is performed with direct image cross-correlation and 3-point Gaussian subpixel estimator of the maximum, with a mask used to restrict the analysis to flow regions. Successive PIV

Table 1 Summary of main experimental variables and derived parameters^a

Run no.	ρ_1 (kg m ⁻³)	ρ_2 (kg m ⁻³)	$\Delta\rho$ (kg m ⁻³)	$(g')_0$ (m s ⁻²)	Q_1 (l s ⁻¹)	Q_2 (l s ⁻¹)	h_b (m)	H (m)	h_r/H	$q^* (Q_1/Q_2)$
EX2	1000.0	1005.1	5.1	0.050	0.0–30.0	6.94	0.43	0.93	0.462	0.0–4.32
EX3	1000.0	1009.6	9.6	0.094	0.0–30.0	6.94	0.45	0.95	0.474	0.0–4.32
EX4	1000.0	1009.6	9.6	0.094	0.0–30.0	6.94	0.35	0.85	0.412	0.0–4.32
EX5	1000.0	1009.6	9.6	0.094	0.0–30.0	2.64	0.35	0.85	0.412	0.0–11.36
EX6	1000.0	1004.7	4.7	0.046	0.0–30.0	2.92	0.354	0.854	0.415	0.0–10.27
EX7	1000.0	1004.7	4.7	0.046	0.0–30.0	6.94	0.349	0.849	0.411	0.0–4.32

^a Expanded details on the individual parametric runs are given in the supplementary material (Table S1)

iterations were conducted with increasing resolutions (two to four iterations were generally conducted depending on the seeding quality). The final correlation box was 20×30 pixels in size, providing spatial resolutions of typically 10 pixels in vertical and 15 pixels in horizontal. This vertical resolution represented 2.5 cm for Dalsa1 (along the sill crest) and 1.2 cm for Dalsa2 (on the down sloping face of the sill). After each PIV iteration, a smoothing interpolation was performed using thin plate splines to eliminate vectors (above a displacement threshold of 1.5 pixels) that were considered false. As this elimination was used only to reduce the search range for the next iteration, the final velocity vector fields obtained from the last PIV measurement had no smoothing applied. Finally the velocity data were linearly interpolated on a regular grid with a 1 cm mesh size to perform statistical analysis. Time intervals for the PIV were chosen to obtain maximum displacements of 5–10 pixels between successive images. With a root-mean-square precision of 0.2 pixel, this corresponds to a relative precision of about 5% of the maximum instantaneous velocity. Since those errors were random with zero mean, the corresponding precision on the mean velocities was somewhat higher. The processing software used is documented in <http://servforge.legi.grenoble-inp.fr/projects/soft-uvmat>, from which the source can be downloaded.

High-resolution density profile measurements were also obtained at key locations both across the sill obstruction and within basin *M* using an array of motorized micro-conductivity probes [8] (C1–C5, Fig. 2a). These micro-conductivity probes traversed vertically through the full depth of the developed two-layer exchange flows at a rate of 5 mm s^{-1} , with full density profiles taken over time periods of 70–90 s for the range of sill submergence depths tested (i.e. $h_b = 0.345\text{--}0.45 \text{ m}$, see Table 1). These detailed density profile measurements enabled mixing characteristics at the interface between the counter-flowing fresh and saline layers to be measured. Corresponding ADV velocity profile measurements were also obtained across the sill, which were used essentially to calibrate the source fresh water volumetric fluxes Q_1 generated within the channel under a range of different centrifugal pumping motor speeds.

4 Internal hydraulic modelling

4.1 Composite Froude number

The critical condition two-layer exchange flow across the sill (Fig. 1) is defined by a relationship between the thicknesses of the counter-flowing fresh and saline water layers [$h_1(x)$ and $h_2(x)$, respectively], their corresponding flow velocities [$u_1(x)$ and $u_2(x)$, respectively], and the reduced gravitational acceleration $g' = g(\rho_2 - \rho_1)/\rho_1 = g(1 - \Gamma)$, where Γ is the density ratio between the fresh and saline waters. Within the Boussinesq approximation, the assumption is made that $(1 - \Gamma) \ll 1$ when defining the critical condition for development of *maximal* two-layer exchange flow. The restricted exchange between the two basins *I* and *M* is controlled by the fresh and saline water volume fluxes, Q_1 and Q_2 , as well as by the total submergence depth $h_b (= h_1 + h_2)$ above the sill obstruction height $h_s(x)$ (see Fig. 1). Internal-flow hydraulic controls for the inviscid flow case might be expected to form at locations A and B in the obstruction side near the saline water source (Fig. 1). However, for the current sill geometry (i.e. constant depth across the sill and in the basins either side), and for exchange flows with net barotropic flow components, these controls are expected to occur over regions rather than at exact locations.

In general, the current study was concerned with investigating exchange flows with net barotropic components (i.e. $q_1 \neq q_2$) generated within the channel to define specific parametric conditions under which blockage of the saline intrusion layer occurs across the sill. Under these conditions, the net barotropic-flow component in the upper layer introduces a mobile “virtual” control [i.e. $F_1^2(x) + F_2^2(x) = 1$; $u_1(x) = u_2(x)$] in a horizontally-constricted flow, which is dependent on the internal-flow head loss. Similarly, in the viscous case of sill flow, the second control [$F_1^2(x) + F_2^2(x) = 1$] at location B (Fig. 1) can be shifted along the sill in the direction of fresh-water source (i.e. towards location C), whilst for strongly dissipative cases, may be shifted beyond the sill area (i.e. into basin I).

At these hydraulic control sections, the composite Froude number G is critical, such that

$$G^2(x) = F_1^2(x) + F_2^2(x) = 1, \quad (1)$$

where $F_1(x)$ and $F_2(x)$ are the local densimetric Froude numbers for the counter-flowing fresh and saline water layers, defined for a rectangular cross-sectional channel as

$$F_1^2(x) = \frac{u_1^2(x)}{g'h_1(x)} \quad \text{and} \quad (2a)$$

$$F_2^2(x) = \frac{u_2^2(x)}{g'h_2(x)}. \quad (2b)$$

The specific volume flux i.e. the volume flux per unit width for the counter-flowing fresh and saline layers can be defined as $q_1 = Q_1/B$ and $q_2 = Q_2/B$. Thus, the corresponding flow velocities can be defined as $u_1(x) = q_1/h_1(x)$ and $u_2(x) = q_2/h_2(x)$, respectively. As such, Eq. (1) becomes

$$G^2(x) = \frac{q_1^2}{g'h_1^3(x)} + \frac{q_2^2}{g'h_2^3(x)} = 1. \quad (3)$$

It is noted here that, within an idealised, inviscid mathematical model representation of the exchange flows across the sill configuration under investigation, the composite Froude number G is constant when both the channel depth and width are constant. However, in the extended, viscous model developed below, G will vary due to mass transfer and internal-flow energy losses across the sill.

4.2 Hydraulic modelling of two-layer exchange flows

For the two-layer exchange flows under consideration here, the relative density difference between the superimposed, counter-flowing, fresh and saline water layers in the internal-flow energy equation is assumed to be small and pressure p_0 at the free-surface is atmospheric. For this inviscid, irrotational flow, the Bernoulli equations of the coupled layers yield the following two-layer flow equations

$$E_1(x) = \frac{1}{2}\rho_1 u_1^2(x) + p_0 + \rho_1 g[h_1(x) + h_2(x) + h_s(x)], \quad \text{and} \quad (4)$$

$$E_2(x) = \frac{1}{2}\rho_2 u_2^2(x) + p_0 + \rho_2 g[h_2(x) + h_s(x)]. \quad (5)$$

In the modelling of two-layer exchange flows, it is customary to define the internal-flow energy equation as

$$E(x) \equiv \frac{E_2(x) - E_1(x)}{\rho_2 g'}. \quad (6)$$

Substituting for $E_1(x)$ and $E_2(x)$ in Eq. (6), the internal-flow energy equation at a particular sill location x becomes

$$E(x) = \left(\frac{u_2^2(x)}{2g'} - \frac{u_1^2(x)}{2g'} \right) + h_2(x) + h_s(x). \quad (7)$$

The flow velocities of the counter-flowing fresh and saline layers, $u_1(x)$ and $u_2(x)$, can also be expressed as corresponding specific flow rates i.e. $q_1 = u_1(x).h_1(x)$ and $q_2 = u_2(x).h_2(x)$, respectively, with Eq. (7) being rewritten as

$$E(x) = K \left(\frac{1}{h_{2,b}^2(x)} - \frac{q^{*2}}{h_{1,b}^2(x)} \right) + h_2(x) + h_s(x), \quad (8)$$

where $K = q_2^2/2g'$ is the flow-rate parameter and $q^* = q_1/q_2$ is the ratio of upper fresh and lower saline layer volume fluxes per unit width. This version of the internal-flow energy equation can be non-dimensionalised in the form

$$E^*(x^*) = K^* \left(\frac{1}{h_{2,b}^{*2}(x^*)} - \frac{q^{*2}}{h_{1,b}^{*2}(x^*)} \right) + h_2^*(x^*) + h_s^*(x^*), \quad (9)$$

where the following non-dimensional quantities are used

$$E^* = \frac{E}{H}, K^* = \frac{q_2^2}{2g'H^3}, x^* = \frac{x}{l}, h_1^* = \frac{h_1}{H}, h_2^* = \frac{h_2}{H}, h_s^* = \frac{h_s}{H} \text{ and } q^* = \frac{q_1}{q_2}. \quad (9a)$$

The maximal flow rate per unit channel width can be derived from the dimensionless Eq. (9) by applying the implicit function differentiation theorem in respect of the dimensionless lower-layer depth h_2^* . In this way, the stratified-flow controlled flow-rate is given by [4]

$$q_2^2(x) = g'H^3 \left/ \left(\frac{1}{h_{2,b}^{*3}(x^*)} + \frac{q^{*2}}{h_{1,b}^{*3}(x^*)} \right) \right. \quad (10)$$

This lower layer flow rate (Eq. 10) corresponds to the bottom saline intrusion across the sill obstruction, while the counter-flowing upper fresh water flow rate can be determined directly from $q_1 = q^*.q_2$. However, in the case of exchange flows with a net barotropic component in the upper freshwater layer, the resulting bi-directional flow can be regarded as *sub-maximal* rather than *maximal* (i.e. two internal hydraulic controls are present).

4.3 Maximal and sub-maximal flow modelling

In the studies of the bi-directional channel flows, the internal hydraulic modelling solutions are usually limited to maximal or sub-maximal exchange flows [1, 4, 24]. Therefore, an essential consideration in the internal hydraulic analysis of two-layer flows has been to determine the location(s) of sections of internal control ($G^2 = 1$). In the present

experimental study, a trapezoidal sill was used to separate the fresh- and salt-water sources and, thus from inviscid internal hydraulic theory, the primary control should be located at the basin *M* end of the trapezoidal sill (i.e. at location A, Fig. 1). In the case of *maximal* exchange flow conditions developing, a second control should be located at the basin *M* end of the trapezoidal-sill crest (i.e. at location B, Fig. 1). According to Armi and Farmer [1], for this maximal exchange-flow case, the two controls are connected by an internally sub-critical branch (i.e. $G^2 < 1$), and separated from the upstream and downstream channel parts by super-critical branches (i.e. $G^2 > 1$). However, with a comparatively large net-barotropic flow component in the surface layer, the second control can also be located in the fresh water source side (i.e. in basin *I*).

The system of internal hydraulic model equations [15, 24] for maximal exchange consists of four relationships and includes, respectively, the critical flow conditions and internal-flow energy equations at the two control locations. As first approximation, this standard approach is used, and the internal-flow model equations at two locations (i.e. at section A and at a section between B and C, Fig. 1) are applied. The hydraulic model equations at location A are

$$G_A^2 = \frac{q_{1,A}^2}{g'h_{1,A}^3} + \frac{q_{2,A}^2}{g'h_{2,A}^3}, \text{ and} \quad (11)$$

$$E_A^* = K_A \left(\frac{1}{h_{2,A}^{*2}} - \frac{q_p^{*2}}{h_{1,A}^{*2}} \right) + h_{2,A}^* + h_{s,A}^* \quad (12)$$

while the hydraulic model equations at a section between locations B and C are

$$G_{BC}^2 = \frac{q_{1,BC}^2}{g'h_{1,BC}^3} + \frac{q_{2,BC}^2}{g'h_{2,BC}^3}, \text{ and} \quad (13)$$

$$E_{BC}^* = K_{BC} \left(\frac{1}{h_{2,BC}^{*2}} - \frac{q_v^{*2}}{h_{1,BC}^{*2}} \right) + h_{2,BC}^* + h_{s,BC}^*. \quad (14)$$

Here, subscripts *A* and *BC* are used to denote the parameters specified for the control locations in basin *M* (i.e. section A, Fig. 1) and across the trapezoidal sill crest (i.e. between sections B and C, Fig. 1), respectively.

A particular goal of the hydraulic modelling presented herein is to investigate the sensitivity of the internal-flow dynamics of the bi-directional stratified flow generated in the rectangular channel configuration incorporating a submerged, trapezoidal, sill obstruction. For this purpose, in addition to the flux ratio q^* of source fresh and saline volume fluxes across the sill, another key non-dimensional parameter is introduced, namely

$$m = Q_{2,BC}/Q_{2,A} = q_{2,BC}/q_{1,A} = 1 - \Delta q_2/q_{2,A}, \quad (15)$$

which represents the loss of mass $\Delta q_2 = (q_{2,A} - q_{2,BC})$ from entrainment of the saline water layer between two control locations A and BC, respectively. The internal-flow head loss is also estimated for different runs according to the formula

$$\Delta E^* = E_A^* - E_{BC}^*. \quad (16)$$

A simple graphical solution of the internal hydraulic model (i.e. Eqs. 11–14) can be used to determine universal solution for the two-layer exchange flow over the trapezoidal

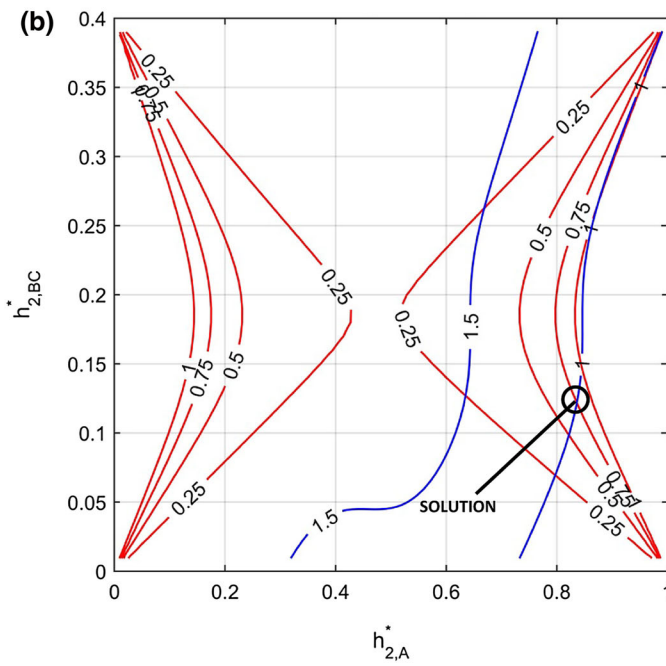
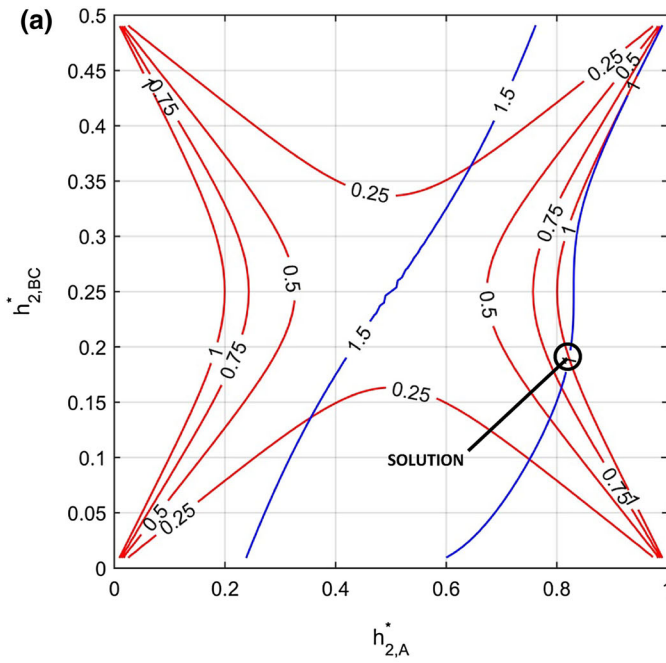


Fig. 3 Internal-flow hydraulic model solution domain for normalised lower layer thicknesses $h_{2,A}^*$ and $h_{2,BC}^*$ (at control sections *A* and *BC*, respectively) for specified q^* : m : ΔE^* values between control sections *A* and *BC* of **a** 1.0: 1.0: 0.0 (i.e. inviscid, zero-net exchange flow with no saline mass transfer to upper fresh layer) and **b** 1.0: 0.75: 0.1 (i.e. viscous, zero-net exchange flow with 25% saline mass transfer ($m = 0.75$) to upper fresh layer)

sill for which a net-barotropic flow component is present (i.e. $q^* \neq 1$). As an example, the solution domain for the normalised lower layer thickness h_2^* at control sections *A* and *BC* (i.e. $h_{2,A}^*$ and $h_{2,BC}^*$) is shown in Fig. 3a for the inviscid exchange flow case with flow ratio $q^* = 1$, internal energy ratio $(E_{BC}^* + \Delta E^*)/E_A^* = 1$ (i.e. blue lines in Fig. 3a), no mass transfer from the lower saline layer (i.e. $m = q_{2,BC}/q_{2,A} = 1$, red lines in Fig. 3a) and no internal-flow head loss between sections *A* and *BC* (i.e. $\Delta E^* = 0.0$). In this case, predictions of the non-dimensional lower-layer depths at the control sections *A* and *BC* are obtained from the intersections of the $(E_{BC}^* + \Delta E^*)/E_A^* = 1$ and $m = 1$ solution curves (see Fig. 3a), with $h_{2,A}^* = 0.822$ (at control section *A*) and $h_{2,BC}^* = 0.190$ (at control section *BC*), respectively. Figure 3b shows a corresponding viscous solution for the exchange flow case with $q^* = 1.0$, a finite mass transfer (i.e. $m = 0.75$) and an internal-flow head loss ($\Delta E^* = 0.1$) specified between sections *A* and *BC*. Here, the solutions for lower layer depths $h_{2,A}^*$ and $h_{2,BC}^*$ are again obtained at the intersection of the $(E_{BC}^* + \Delta E^*)/E_A^* = 1$ (blue line, Fig. 3b) and $m = 0.75$ (red line, Fig. 3b) solution curves, with $h_{2,A}^* = 0.836$ (at control section *A*) and $h_{2,BC}^* = 0.122$ (at control section *BC*). As expected, the slope of interface between the two control sections (i.e. *A* and *BC*), has increased when compared to the corresponding slope of the inviscid case (i.e. due to larger depth $h_{2,A}$ in basin *M* and a lower depth $h_{2,BC}$ over the sill). This extended internal hydraulic model (accounting for both lower layer entrainment and head-losses) can be applied straightforwardly to the cases of net barotropic flow in the lower saline ($q_1 < q_2$, $q^* < 1$) and upper fresh ($q_1 > q_2$, $q^* > 1$) layers. The extended internal-flow hydraulic modelling approach will be used to estimate the limits for mass exchanges and internal-flow head losses in the present experiments.

5 Experimental results

5.1 Description of exchange flow and saline blockage conditions

Within the current experimental study, the development of bi-directional stratified flows across the sill obstruction were measured for both net-barotropic flows in the upper freshwater ($q^* > 1$) and lower saline ($q^* < 1$) layers using PIV measurements. In this context, Figs. 4 and 5 present examples of synoptic, time-averaged velocity vector fields and corresponding colour maps of the horizontal *U* velocity component for these net exchange flows generated across the horizontal sill and down the inclined slope into impoundment basin *I*. It was noted during PIV analysis that the measured velocity fields at specific *x* locations along the sill, and on the sill crest at the freshwater impoundment basin *I*, were distorted significantly by viewing obstructions in the transparent flume wall sections and the positioning of micro-conductivity density probes at these locations. As such, the velocity vector fields in these regions have been blanked out and discounted from subsequent quantitative analysis of the exchange flows. For run EX2, Fig. 4a–c indicate that the effect of increasing the upper source freshwater flow rate Q_1 in incremental steps (i.e. $Q_1 = 0, 12$ and 30 l s^{-1} shown) for a prescribed saline water volume flux

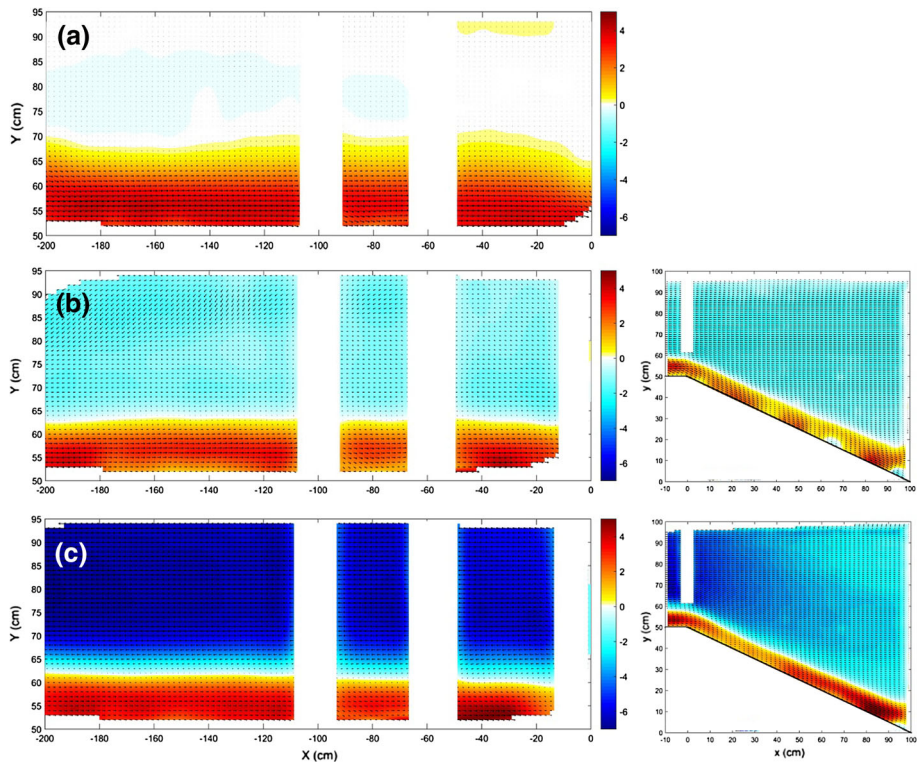


Fig. 4 Synoptic PIV velocity fields consisting of (u, v) velocity vectors and $u(x, z)$ colour maps for run EX2 showing stratified exchange flows across the sill obstruction and on downslope into impoundment basin *I* for $q^* : q_1^2/(g'h_b^3)$ values of **a** 0.0: 0.0; **b** 1.73: 6.698×10^{-3} ; and **c** 4.32: 4.186×10^{-2}

$Q_2 = 6.94 \text{ l s}^{-1}$, results in bi-directional stratified flow conditions with reducing lower layer thickness h_2 , defined by the $u = 0$ contour elevation, and increased velocity in the upper fresh layer (i.e. $u_1 \rightarrow 6 \text{ cm s}^{-1}$). However, the corresponding lower saline layer velocity u_2 does not diminish significantly (i.e. $u_2 \rightarrow 4 \text{ cm s}^{-1}$) under increasingly dominant upper fresh water flows and bi-directional stratified flow conditions persist across the sill and down the slope into basin *I* for all q^* values tested (i.e. $q^* = 0 \rightarrow 4.32$). By contrast for run EX7, Fig. 5a–d show both a general reduction in lower layer thickness h_2 and velocity u_2 as the net-barotropic forcing in the upper fresh layer increases. Indeed, it is shown in Fig. 5d that the saline intrusion is completely blocked across the sill under the strongest net-barotropic forcing conditions in the upper freshwater layer (i.e. $q^* = 3.75$ and 4.32). It is noted that the only significant parametric difference between runs EX2 and EX7 is the total flow depth H and, hence, the total submergence depth h_b of the horizontal sill (i.e. $h_b = 0.43 \text{ m}$ and 0.349 m , respectively), indicating its parametric significance to conditions under which the saline intrusion is blocked.

In this context, Fig. 6 defines the parametric conditions under which saline blockage occurs, plotting the non-dimensional source freshwater volume flux $q_1^2/(g'_0 h_b^3)$ versus the volume flux ratio $q^* = q_1/q_2$. The magnitude of $q_1^2/(g'_0 h_b^3)$, which is equivalent to densimetric Froude number F_1 for the freshwater layer when $h_1 = h_b$, is shown to control the parametric conditions under which the saline intrusion layer is blocked. This occurs at a

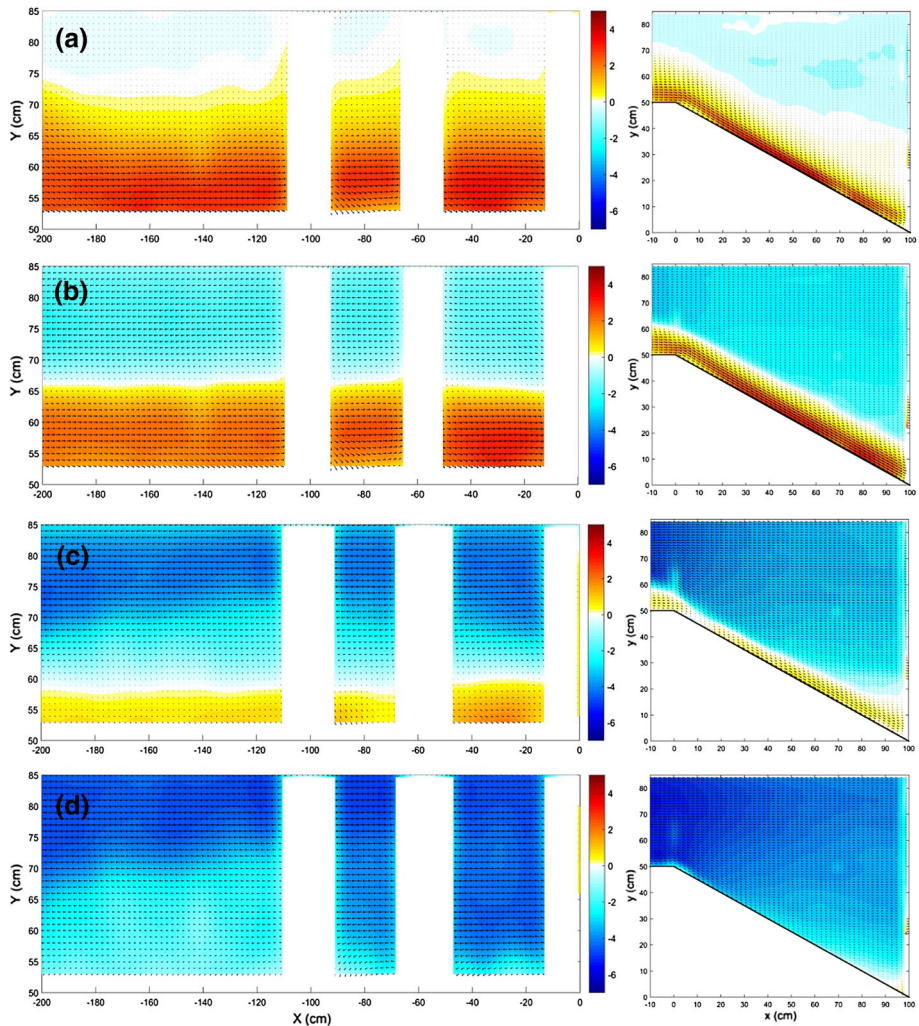


Fig. 5 Synoptic PIV velocity fields consisting of (u, v) velocity vectors and $u(x, z)$ colour maps for run EX7 showing stratified exchange flows across the sill obstruction and on downslope into impoundment basin *I* for q^* : $q_1^2/(g'_0 h_b^3)$ values of **a** 0.0: 0.0; **b** 1.15: 3.978×10^{-3} ; **c** 3.03: 2.741×10^{-2} ; **d** 4.32: 5.594×10^{-2}

critical value $q_1^2/(g'_0 h_b^3) > \sim 0.125$ irrespective of the relative magnitude of the fresh and saline volume flux ratio q^* (Fig. 6). In a dimensional sense, this is somewhat surprising as intuitively it might have been expected that lower saline volume fluxes q_2 across the sill (e.g. run EX5) could be blocked by correspondingly reduced fresh water volume fluxes q_1 , thus maintaining the same critical net-barotropic flow condition in the upper freshwater layer (i.e. $q^* > 1$) for saline blockage to occur. However, bi-directional stratified flows are shown to develop in all runs where $q_1^2/(g'_0 h_b^3) \leq 0.1$ over a corresponding q^* range of 0 to 11.36 (Fig. 6), suggesting that saline layer blockage requires a specific parametric combination of high freshwater volume flux q_1 and lower submergence depth h_b and reduced gravity g'_0 values (e.g. runs EX6 and EX7). In this context, a reduction in g'_0 and/or h_b appears to increase shear-driven interfacial mixing across the sill between the counter-

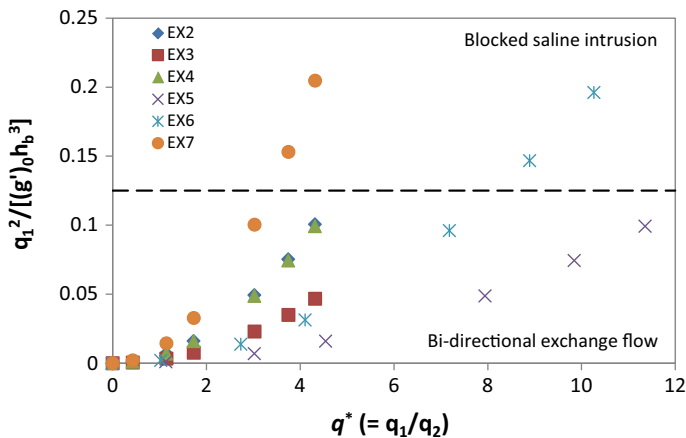


Fig. 6 Parameter space for normalised upper freshwater volume flux $q_1^2/[(g')_0 h_b^3]$ versus fresh-saline volume flux ratio $q^* = (q_1/q_2)$, indicating the parametric region within which saline intrusion layer blockage occurs (i.e. at $q_1^2/[(g')_0 h_b^3] \geq \sim 0.125$ for $q^* = 0 \rightarrow 12$)

flowing fresh and saline water layers, leading to enhanced entrainment of saline water by the dominant upper fresh water layer, especially at higher $q^* > 1$ values. This is also evidenced by the significant reduction in, and eventual disappearance of, the $u = 0$ contour elevation in Fig. 5 (run EX7) with increasing q^* values. By contrast, the corresponding run (EX2, Fig. 4) at the higher submergence depth h_b indicates a less pronounced reduction in the $u = 0$ contour elevation with increasing q^* values, suggesting the exchange flow is more stably stratified with less interfacial mixing and entrainment of saline water into the dominant counter-flowing fresh water layer observed even under high $q^* \gg 1$ values.

5.2 Quantitative analysis of PIV measurements

Figure 7 shows example plots of U velocity profiles derived from the synoptic PIV velocity fields at specific x locations across the sill (i.e. $x = -120, -80$ and -30 cm) for the range of q^* values tested. The majority of these profiles indicate bi-directional exchange flows developing between the intruding lower saline water layer (i.e. $u > 0$) and counter-flowing upper freshwater layer (i.e. $u < 0$), except under conditions with no upper freshwater volume flux (i.e. $q^* = 0$) or where the saline water intrusion is fully blocked by dominant net-barotropic flow conditions in the upper freshwater layer. As previously indicated in the PIV vector fields (Figs. 4, 5), the elevation of the $u = 0$ velocity interface between the counter-flowing layers is shown to reduce as the upper fresh water layer velocity u_1 increases under increasing q^* values. However, within run EX2 (Fig. 7a), the lower saline intrusion layer is shown to remain relatively persistent both in terms of thickness h_2 and velocity u_2 across the sill for all q^* values tested. This suggests that, although the net barotropic flows generated in the upper fresh layer has a pronounced dynamic influence on the saline intrusion, it is not sufficient to block it completely. Run EX7 (Fig. 7b) reveals similar parametric trends of increasing and reducing upper and lower layer velocities u_1 and u_2 , respectively, and decreasing saline layer thickness h_2 as the flow ratio q^* is increased. In this case, however, the parametric dependence on q^* results in the complete blockage of the saline water intrusion (i.e. $h_2, u_2 \rightarrow 0$) under the highest net-barotropic flow component generated in the upper freshwater layer (i.e. $q^* = 3.75$ and 4.32). It is

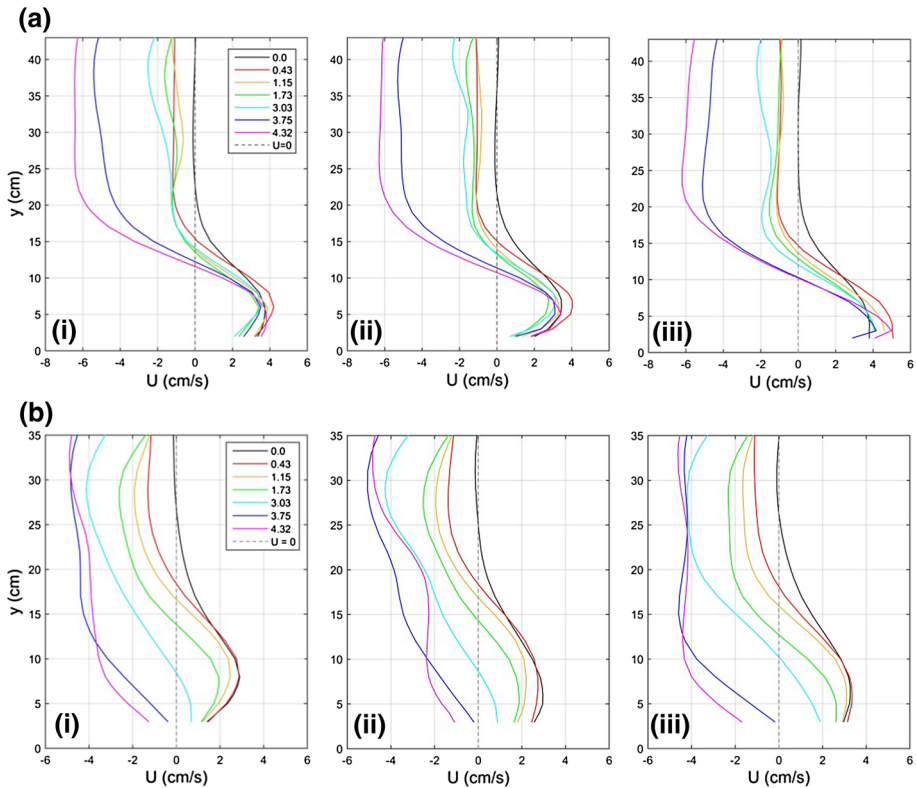


Fig. 7 Depthwise profiles of the horizontal velocity component u for bi-directional exchange flows generated across the sill (derived from synoptic PIV velocity fields) for runs **a** EX2 and **b** EX7. Velocity profiles shown are obtained at longitudinal positions (i) $x = -120$ cm; (ii) $x = -80$ cm; and (iii) $x = -30$ cm for the values of the fresh-saline flux ratio q^* shown

noted that the key parametric difference between runs EX2 (Fig. 7a) and EX7 (Fig. 7b) is the sill submergence depth h_b (i.e. $h_b = 0.43$ m and 0.349 m, respectively). As such, the observed variation in the $u = 0$ interface height in both cases (i.e. $h_2 = 15 \rightarrow 10$ mm and $18 \rightarrow 0$ mm, respectively) for increasing q^* values is therefore controlled primarily by the submergence depth h_b , thus confirming its parametric importance in the blockage of saline intrusions across the sill.

It is possible to determine the local upper \hat{q}_1 and lower \hat{q}_2 layer volume fluxes (per unit width) at specific x positions along the sill through integration of the velocity profiles shown in Fig. 7, i.e.

$$\hat{q}_1 = \int_{z=h_2}^{h_b} u dz \approx \bar{u}_1(h_b - h_2) \quad (\hat{Q}_1 = \hat{q}_1 B), \text{ and} \quad (17)$$

$$\hat{q}_2 = \int_{z=0}^{h_2} u dz \approx \bar{u}_2 h_2 \quad (\hat{Q}_2 = \hat{q}_2 B). \quad (18)$$

In this way, calculations of the local upper and lower layer volume fluxes, \hat{Q}_1 and \hat{Q}_2 , respectively, along with corresponding measurements of layer thicknesses h_1 and h_2 , can be determined at various positions along the sill. A summary of these calculated fresh and saline volume fluxes \hat{Q}_1 and \hat{Q}_2 , and corresponding layer thicknesses h_1 and h_2 are provided in the supplementary material (Table S2) at locations $x = -30$ and -200 cm along the sill for runs EX2, EX3, EX6 and EX7. It is interesting to note that these local fluxes are, in general, significantly lower than the specified fresh and saline water flows Q_1 and Q_2 at source. This is likely to be in part due to uncertainties in predicting \hat{Q}_1 and \hat{Q}_2 (Eqs. 17, 18) from single bi-directional velocity profiles along the sill crest. However, it is informative to investigate how the local flux ratio \hat{Q}_1/\hat{Q}_2 varies along the sill under varying parametric conditions to provide insight into the influence of net-barotropic flow conditions on the volume flux changes in the upper fresh and lower saline layers across the sill. In this context, Fig. 8 plots a comparison of the local flux ratios \hat{Q}_1/\hat{Q}_2 at both sill locations (i.e. $x/l_s = -1.0, -0.15$), excluding only the parametric conditions under which (i) no fresh water flow is specified, i.e. $\hat{Q}_1/\hat{Q}_2 = 0$, and (ii) full saline blockage occurs, i.e. $\hat{Q}_1/\hat{Q}_2 \rightarrow \infty$. This plot indicates firstly that the range of \hat{Q}_1/\hat{Q}_2 values at the basin M end of the sill (i.e. $x/l_s = -1.0$) agree reasonably well with the $q^* = Q_1/Q_2$ range specified at the fresh and saline sources (i.e. $q^* = 0.43$ – 10.27 for runs EX1, 2, 6 and 7). By contrast, the corresponding \hat{Q}_1/\hat{Q}_2 values at impoundment I end of the sill (i.e. $x/l_s = -0.15$) are typically higher for all bi-directional stratified flow conditions, become significantly higher (up to ~ 60) for exchange flows with large net-barotropic flow components in the upper fresh water layer. This apparent increase in \hat{Q}_1/\hat{Q}_2 values in the direction of the saline intrusion is clearly indicative of the reduction in \hat{Q}_2 values, of up to 86%, that occurs due to interfacial mixing and entrainment of saline water into the dominant, counter-flowing upper freshwater layer (i.e. under high q^* conditions). By contrast, the influences of \hat{Q}_1 flux

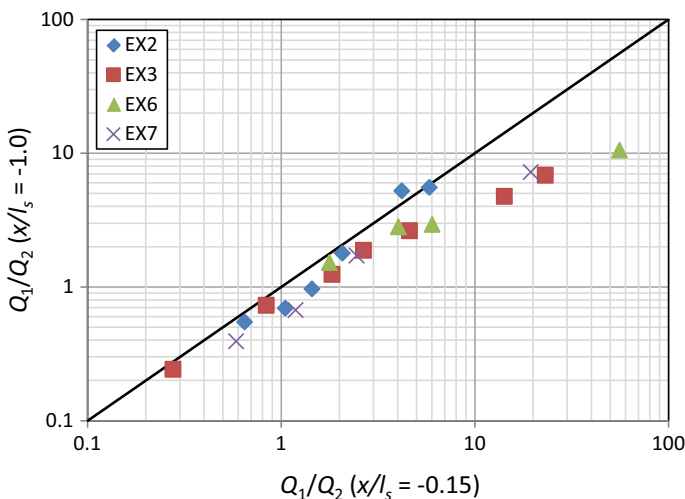


Fig. 8 Comparison of local fresh-saline flux ratios measured across the sill at $x/l_s = 1.0$ (i.e. basin M end) and $x/l_s = -0.15$ (i.e. towards impoundment I end) showing relative increase in \hat{Q}_1/\hat{Q}_2 in direction of saline water intrusion (i.e. $x/l_s = -1.0 \rightarrow -0.15$)

changes in the upper fresh water layer are less obvious with some runs indicating the expected increase in \hat{Q}_1 values in direction of flow, due to added mass from the lower saline layer entrainment, while others either indicate negligible flux changes or even a flux reduction in the flow direction.

5.3 Analysis of density profiles

Density profiles for the exchange flows generated across the sill were measured via micro-conductivity probes located at $x/l_s = 0.0, -0.25$ and -0.5 . Figure 9a, b presents the raw density profiles from runs EX2 and EX3 for the values of the fresh to saline volume flux ratio q^* shown. Both these runs indicate significant levels of mixing throughout the lower saline intrusion layer at $x/l_s = 0.0$ [Fig. 9a(iii), b(iii)] as it spills over the sill crest into impoundment basin *I*. At $x/l_s = -0.25$ and -0.5 , however, mixing is confined to the interfacial shear region between the counter-flowing fresh and saline layers, with some evidence of denser water entrainment into the upper freshwater layer [e.g. Figs. 9a(i), (ii), b(i), (ii)], while the saline intrusion layer appears to have a relatively stable density structure. It is noted here that the lower layer density increases over the first three q^* conditions, indicating that the full density excess for the bi-directional stratified flow is not established over these q^* values. This is possibly due to mixing and dilution of the inflowing saline water source flux during the initial infilling stage within basin *M*. Figure 9c presents raw density profiles for run EX7 at equivalent x/l_s positions along the sill. These profiles again show significant mixing in the lower saline intrusion layer, and especially at $x/l_s = 0$, where large instabilities in the density profiles are observed for exchange flow conditions where the net barotropic flow component is approximately zero [i.e. $q^* = 1.15$, Fig. 9c(iii)]. This may be indicative of the large-scale interfacial erosion and entrainment of the lower saline layer at this location by the counter-flowing freshwater layer. At higher q^* values (i.e. strong barotropic flow component in the upper freshwater layer), the saline intrusion layer diminishes and is removed completely at $q^* = 3.75$ and 4.32 , in accord with the corresponding PIV measurements shown in Fig. 5d. By contrast, density profiles at $x/l_s = -0.25$ and -0.5 are again more stably stratified at q^* values up to 1.73 [i.e. Figure 9c(i), (ii)], while increased levels of mixing and dense water entrainment are into the upper freshwater layer are observed at higher q^* values as the lower saline intrusion layer diminishes in thickness, before eventually disappearing at $q^* = 4.32$.

In order to investigate the level of mixing associated with bi-directional stratified flows with varying net barotropic components across the sill, the density profiles measured at the three x/l_s locations were sorted vertically into an equivalent stable density profile for each of the different q^* conditions tested. Examples of these sorted density profiles are plotted non-dimensionally in Fig. 10a–c for runs EX2, EX3 and EX7, respectively, as the density excess $\rho' = [\rho(z) - \rho_1]/(\rho_2 - \rho_1)$ versus the normalised submergence depth z/h_b above the sill at location $x/l_s = -0.25$ for the range of q^* values tested. The elevations of the $\rho' = 0.2, 0.5$ and 0.8 isopycnals are plotted on individual sorted density profiles, providing an indication of the mixing layer thickness at the different sill locations [3] for different q^* values. The vertical separation of these isopycnals is typically largest at (i) low q^* values, most probably due to initial saline-fresh water mixing in basin *M* during filling, and (ii) higher q^* values, due to increased interfacial mixing and entrainment of the lower saline intrusion layer by strong net barotropic flow components in the upper freshwater layer. This is illustrated in Fig. 10c (i.e. run EX7, $x/l_s = -0.25$) where the isopycnal separation in the generated exchange flows is greatest at $q^* = 0, 3.03$ and 3.75 , prior to the blockage

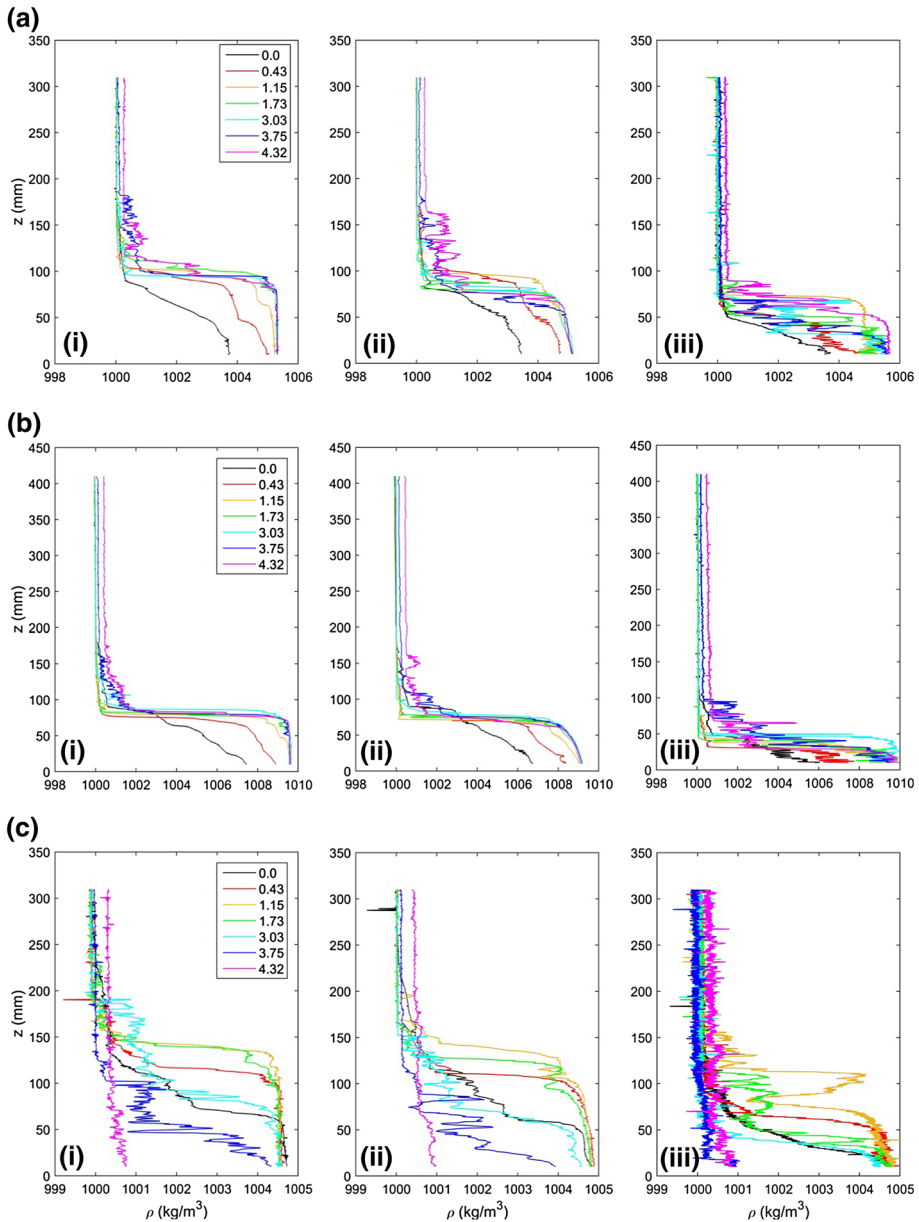


Fig. 9 Raw density profile measurements obtained by micro-conductivity probes in runs **a** EX2, **b** EX3 and (EX7) at longitudinal positions of (i) $x = -100$ cm; (ii) $x = -50$ cm; and **c** $x = 0$ cm across the sill for the exchange flows generated with the fresh-saline flux ratios q^* as shown

of the saline intrusion layer at $q^* = 4.32$. It is also interesting to note that the elevation of the $\rho' = 0.5$ isopycnal rises initially with increasing q^* (i.e. $q^* = 0 \rightarrow 1.15$) before reducing with further increasing q^* values (i.e. $q^* = 1.15 \rightarrow 3.75$). It is anticipated that the former effect is due to the less dominant fresh water layer acting to slow down the saline

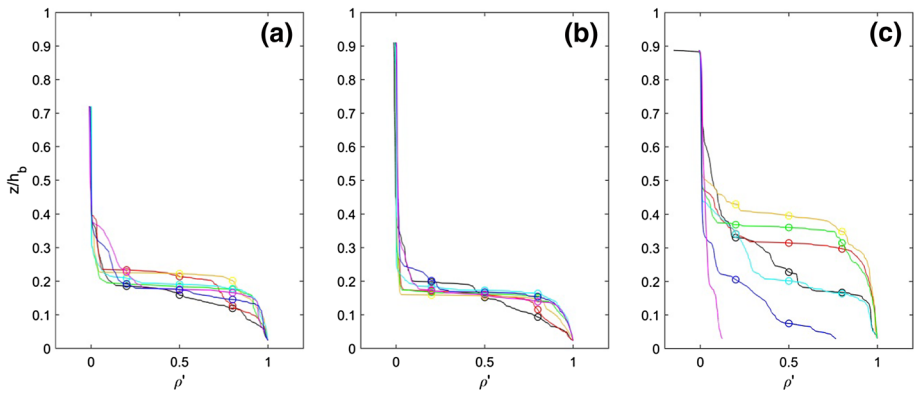


Fig. 10 Vertically-sorted and normalised density excess profiles $\rho' = [\rho(z) - \rho_1]/(\rho_2 - \rho_1)$ plotted versus the non-dimensional depth z/h_b above sill crest at longitudinal position $x/l_s = -0.25$ for runs **a** EX2, **b** EX3 and **c** EX7. Isopycnal elevations for $\rho' = 0.2, 0.5$ and 0.8 are plotted on each sorted profile for comparison purposes. (Note: colour coding of profiles is the same as in Fig. 9 for different fresh-saline flux ratio q^* values)

water intrusion layer across the sill, which for a given flux q_2 will result in the intrusion layer becoming thicker. Conversely, under more dominant upper fresh water flows (i.e. higher q^* values), the mixing and entrainment of saline water at the interface will reduce the overall thickness of the saline intrusion layer, prior to its complete removal at $q^* = 4.32$. In comparison, for runs EX2 and EX3 (Fig. 10a, b) where ultimately saline blockage does not occur, both the isopycnal separation and elevation of the $\rho' = 0.5$

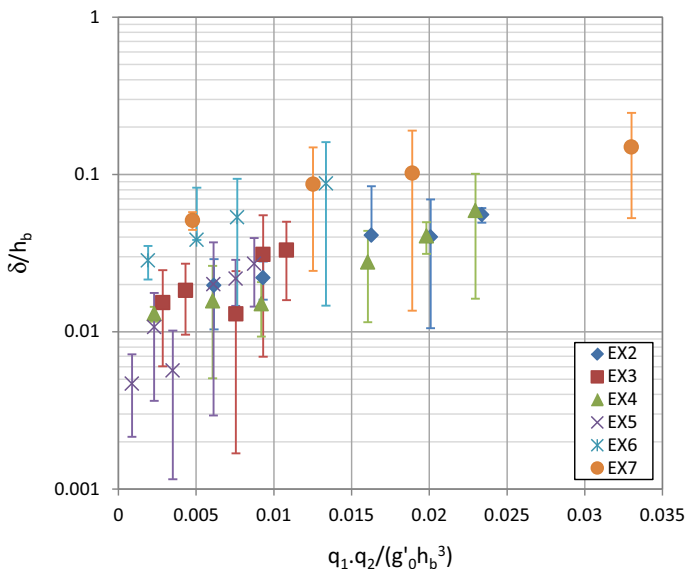


Fig. 11 Normalised isopycnal separation thickness $\delta/h_b [= (z_{(\rho'=0.2)} - z_{(\rho'=0.8)})/h_b]$ plotted versus a non-dimensional exchange flow parameter $q_1 q_2 / (g'_0 h_b^3)$ for all runs in which bi-directional exchange flows were generated across the sill. δ/h_b values shown are averaged for three density profiles obtained across sill (i.e. $x/l_s = -0.5, -0.25$ and 0.0), with error bars showing ± 1 standard deviation for the three δ/h_b values

isopycnal are more consistent over the range of q^* values tested. Figure 11 shows the normalised isopycnal separation thicknesses δ/h_b (where δ is the elevation difference between the $\rho' = 0.2$ and 0.8 isopycnals) for all runs in which bi-directional exchange flows are generated across the sill plotted versus a modified densimetric Froude number $q_1^2/(g'_0 h_b^3)(1/q^*) = q_1 q_2/(g'_0 h_b^3)$. This non-dimensional exchange flow parameter takes account of both the dominant role of the upper fresh water layer in generating interfacial mixing and the relative magnitude of the fresh-saline volume flux ratio q^* . These δ/h_b values are averaged across the three density probe locations, with the error bars shown representing the standard deviation in these measurements. The figure shows a general trend of increasing δ/h_b values with increasing $q_1 q_2/(g'_0 h_b^3)$, both within individual runs and over the range of parametric conditions tested. This indicates that, for a specific prescribed saline volume flux q_2 , an increase in fresh water volume flux q_1 and/or a reduction in reduced gravity g'_0 or submergence depth h_b tends to result in increased interfacial mixing (i.e. larger isopycnal separation), with correspondingly higher variability on these measurements (i.e. larger error bars). It is also noted that the largest δ/h_b values [up to $O(10^{-1})$] are typically obtained for the two runs (EX6 and EX7) in which the saline intrusion layer was blocked at high q^* values.

It is observed that some density profiles highlight significant density inversions [e.g. Fig. 9c(iii)] that are indicative of large instabilities being generated at the interface between the counter-flowing fresh and saline layers, particularly close to the basin *I* end of the sill (i.e. $x/l_s = 0$). These interfacial instabilities can be defined quantitatively by the Thorpe overturning length scale L_T [23], which is a measure of the vertical scale of short wave instabilities, such as Kelvin–Helmholtz overturning motions, associated with shear-induced interfacial mixing. It is defined as the root-mean-square of vertical displacements required to re-order the measured density profile such that the resulting stratification becomes gravitationally stable. In the current study, where the time scales of short wave instabilities and overturning motions are significantly shorter than the density profiling time scale (i.e. 70–90 secs), L_T is used only as a semi-quantitative measure of the ensemble-averaged mixing characteristics at the three x/l_s positions along the sill crest. Furthermore, estimations of L_T can be subject to significant errors from noise in density profiles [11]. Hence, its prediction is limited to the re-ordered density profiles between isopycnals $\rho' = 0.2$ and 0.8 (see Fig. 10). In this context, Fig. 12 presents normalised Thorpe length scales L_T/h_b plotted versus q^* for runs EX2, EX3 and EX7. These plots show a general increase in L_T/h_b with q^* , again confirming that larger interfacial instabilities are generated under stronger net barotropic flow conditions in the upper freshwater layer (i.e. $q^* \gg 1$). In Fig. 12a, b, the L_T/h_b values increase by an order of magnitude [$O(10^{-2} \rightarrow 10^{-1})$] over the range of q^* values tested (i.e. $q^* = 0 \rightarrow 4.3$), with no clear dependence on x/l_s location. By comparison, Fig. 12c shows that estimated L_T/h_b values in run EX7 are significantly higher at $x/l_s = 0$ than at $x/l_s = -0.25$ or -0.5 for q^* values of 0.43, 1.15 and 1.73, with Thorpe length scales at $x/l_s = 0$ approaching up to half the total sill submergence depth (i.e. $L_T/h_b \rightarrow 0.4$ – 0.5). This may indicate that the degradation and eventual blockage of the saline intrusion layer across the sill is initiated by large scale instabilities forming at the basin *I* end of the sill crest, leading to bulk mixing and entrainment, under dominant fresh water flows with strong net barotropic components (i.e. $q^* \gg 1$). By contrast, more general shear-induced interfacial mixing between stable counter-flowing fresh and saline water layers is characterised by smaller L_T/h_b values under all q^* conditions [e.g. run EX3, Fig. 12b]. These results are also in general accord with Fig. 11, where the largest isopycnal separation δ/h_b values were generally obtained in runs that resulted in the eventual blockage of the saline intrusion layer, while lower δ/h_b values were obtained

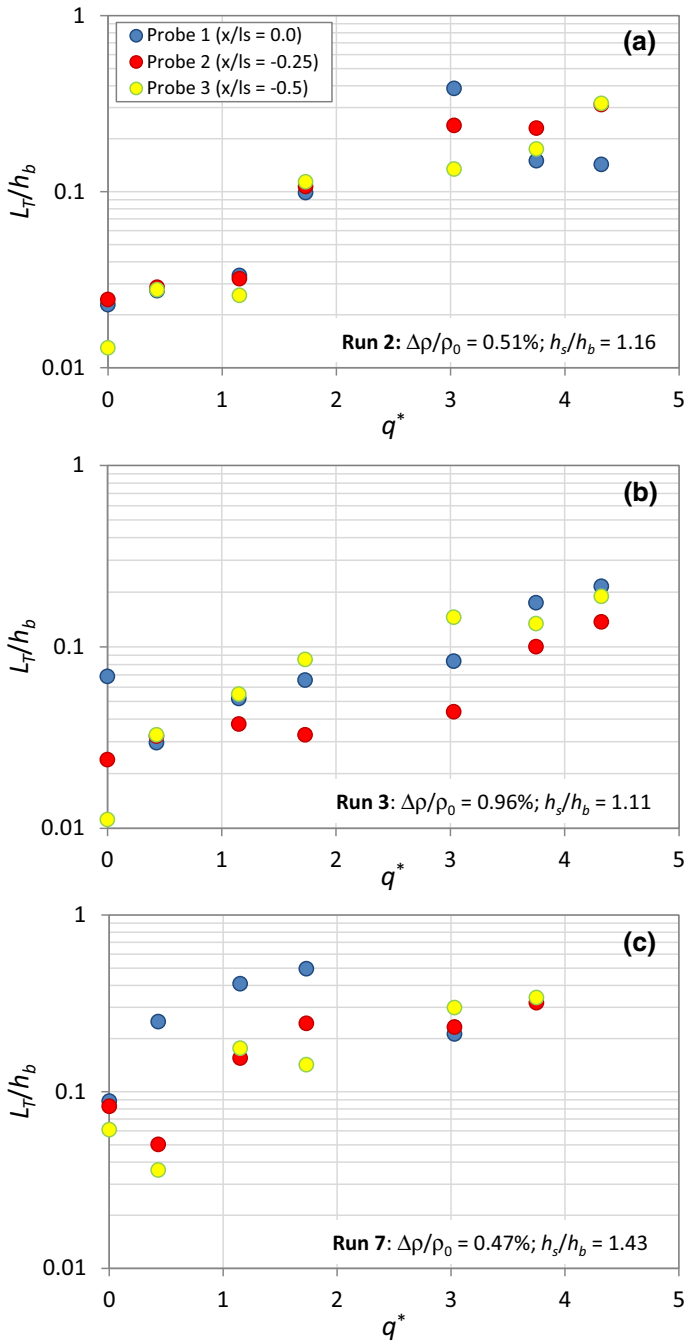


Fig. 12 Normalised Thorpe overturning length scales L_T/h_b plotted versus fresh-saline flux ratio q^* for runs **a** EX2, **b** EX3 and **c** EX7. These plots provide a measure of the vertical scale of short wave instabilities (i.e. Kelvin–Helmholtz overturning motions) from density profiles measured at $x/l_s = -0.5, -0.25$ and 0 along the sill

Fig. 13 Longitudinal variations in the estimated composite Froude number ($G = F_1 + F_2$) [Eq. (19)] along the sill crest ($x/l_s = -1.0 \rightarrow 0.0$) for runs **a** EX2, **b** EX3, **c** EX4, **d** EX6 and **e** EX7 for the values of fresh-saline flux ratio q^* as shown. Horizontal error bars indicate the sill region extent over which each spatially-averaged G value is attained, while the vertical error bars indicate ± 1 standard deviation in these predicted spatially-averaged G values

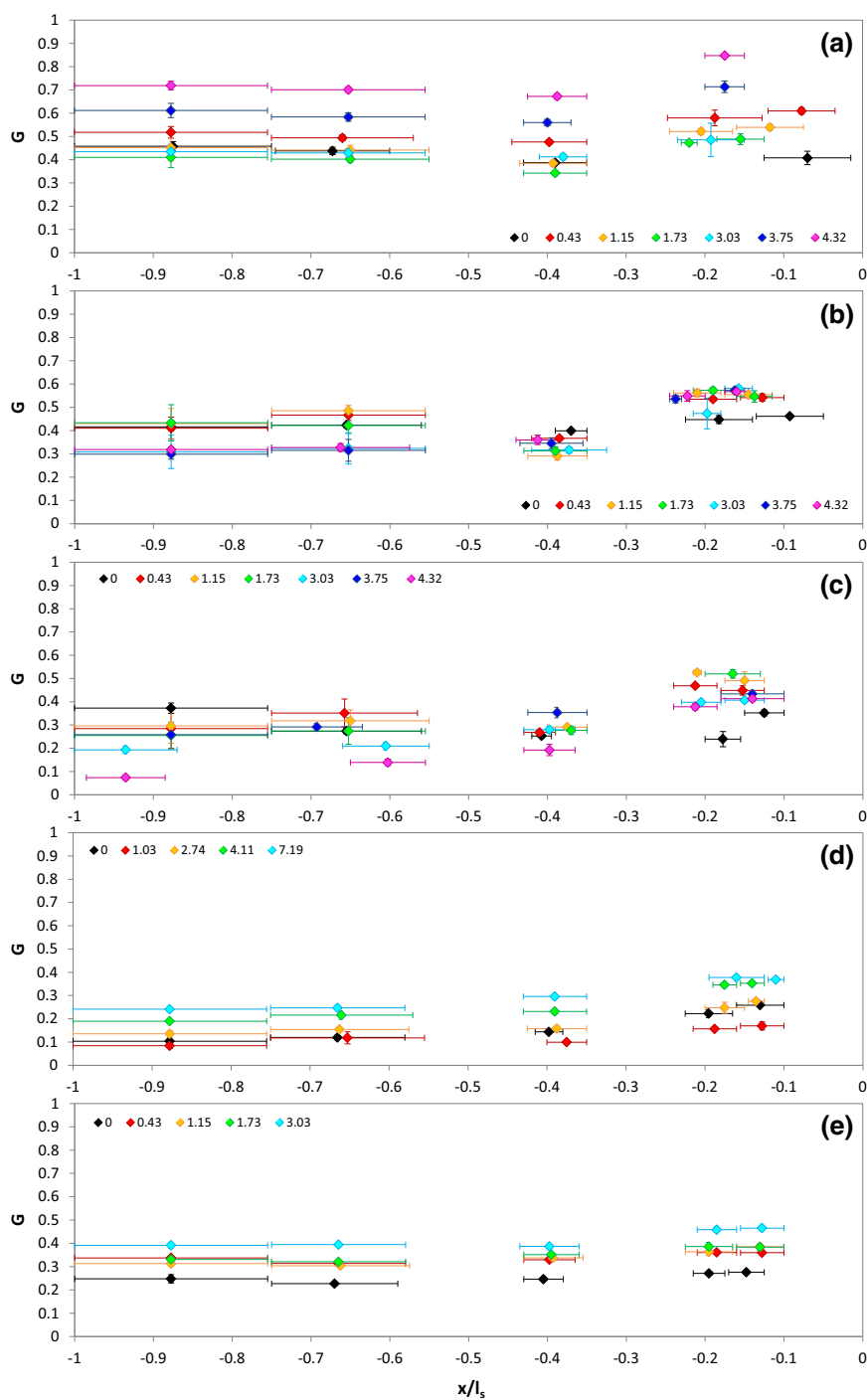
under parametric runs leading to more stably stratified two-layer exchange flows. It is recognised here that both δ/h_b and L_T/h_b indicate similar increasing trends with q^* values.

5.4 Composite Froude number

The composite Froude number G for the two-layer exchange flows generated across the sill was calculated for each run, following Eq. (3), as

$$G^2(x) = \frac{u_1^2(x)}{g'h_1(x)} + \frac{u_2^2(x)}{g'h_2(x)}, \quad (19)$$

where $u_1^2(x)$ and $u_2^2(x)$ are representative layer-averaged velocities for the counter-flowing fresh and saline water layers, respectively. These are obtained by integrating PIV-derived velocity profiles (e.g. Fig. 7) above and below the $u = 0$ contour elevation at all x positions along the sill and dividing by the corresponding fresh and saline layer thicknesses $h_1(x)$ and $h_2(x)$. The reduced gravitational acceleration g' term in Eq. (19) is also based on local density profile measurements across the sill, detailed in the supplementary material (Table S2). As such, Fig. 13 shows the spatial variation in estimated composite Froude numbers G across the sill (i.e. $x/l_s = -1.0 \rightarrow 0.0$) for individual runs and the range of fresh-saline flux q^* ratio values shown in each plot. Within Fig. 13, the horizontal error bars represent the sill region over which G values were averaged, while the vertical error bars represent ± 1 standard deviation in the individual G values contributing to the spatially-averaged G values plotted. Within all runs, it is apparent that the estimated composite Froude numbers remain subcritical (i.e. $G^2 < 1$) at all locations along the sill for all q^* values. The largest G values (i.e. $G \approx 0.55\text{--}0.85$) are obtained in run EX2 (Fig. 13a) under the highest q^* values (i.e. $q^* = 3.75$ and 4.32), within which bi-directional exchange flows were generated across the sill even under the strongest net-barotropic forcing in the upper freshwater layer (see Fig. 4c). By contrast, smaller G values are typically estimated in all other runs over the range of q^* values in which bi-directional exchange flows are generated (Fig. 13b–e). The fresh-saline flux ratio q^* itself demonstrates a weak influence on the estimated G values (i.e. G increases as q^* increases), especially within runs EX6 and EX7 (Fig. 13d, e), where the saline intrusion layer becomes increasingly diminished in thickness h_2 , then completely blocked, for increasing q^* values (Fig. 5). It is also observed that the estimated G values tend to increase towards the impoundment I end of the sill, due primarily to the observed increase in the lower saline layer velocity u_2 and reduction in layer thickness h_2 as sill crest location $x/l_s \rightarrow 0$ (e.g. see Fig. 4). In general, as the findings suggest that the internal-flow remains subcritical (i.e. $G^2 < 1$) along the full length of the sill, the second internal hydraulic control point ($G^2 = 1$) must be positioned at some location within the freshwater impoundment I . This finding is in accord with Laaneau et al. [16], who found that for net exchange flows in a laterally-confined river channel, where the dominant barotropic component was in the upper freshwater layer, the location of the second hydraulic control could be displaced towards the freshwater source. It should be noted that while the spatially-averaged G values plotted in Fig. 13 are representative of the local exchange flow conditions generated across the sill, these specific values should



only be considered as estimates. This is due to both the velocity and density profile measurements, used in the estimation of G , varying significantly from the idealised two-layer exchange flow condition. As such, they include uncertainties associated with turbulent fluctuations and interfacial wave activities.

6 Analytical modelling

Modelling of exchange flows over sill obstructions is usually restricted to two-layer cases, where flows in the upper and lower layers are in opposite directions. For idealised maximal exchange flows [24], two critical-flow sections ($G^2 = 1$) are assumed to form in the obstructed channel; one at location A in basin M and the second on the sill crest between locations B and C (see Fig. 1). However, sub-maximal exchange can also occur when only one critical-flow section exists, and is established at location A in basin M . Within the current experimental study, the second control is expected to be located outside of the trapezoidal sill area, toward the fresh-water source (i.e. in basin I , Fig. 1). This is confirmed by the estimated composite Froude numbers across the sill crest (i.e. Figure 13), which were shown to remain subcritical (i.e. $G^2 < 1$) throughout. The experimental results also show that, under certain parametric conditions (Fig. 6), the dynamic blocking of the saline water intrusion can occur across the sill. This is analogous to “salt-wedge” behaviour in stratified estuaries, which has been modelled experimentally [22] and also been observed from flow velocity profiles and density front observations in a river channel [16]. The dynamic blocking of saline water intrusions in regions of restricted exchange remains relatively poorly understood as it involves complex internal-flow dynamics and forcing due to the interfacial mixing and entrainment between the counter-flowing fresh and saline layers. In the idealised analytical two-layer hydraulic model (i.e. inviscid flow case), upper or lower layer blockage can be simulated by reducing or increasing the fresh-saline flux ratio q^* significantly (i.e. $q^* \rightarrow 0$ and $1/q^* \rightarrow 0$, respectively) [1]. Within the current experiments, however, the dynamic blocking condition for the saline intrusion layer across the sill occurs at a finite value of $1/q^* < 1$. As such, an additional complexity arises from the appropriate model representation of interfacial mixing and entrainment processes in a non-idealised two-layer hydraulic model (i.e. viscid flow case). Consequently, the extended internal-flow hydraulic model (detailed in Sect. 4) allows specification both of an internal-flow head loss ΔE^* and a mass transfer coefficient m from the lower saline layer between the two control ($G^2 = 1$) points A and BC (Fig. 1). This permits determination of the dynamic conditions for saline intrusions under restricted, two-layer exchange flows across the submerged sill obstruction, which can be compared directly with experimental observations of the $u = 0$ interface height across the sill.

Essentially, two dimensionless sill submergence depths $h_s^* = h_s/H = (1 - h_b/H) = 0.532$ (runs EX2 and EX3) and 0.588 (runs EX4-EX7) were considered in the current experimental study of exchange flows with varying net-barotropic flow components (i.e. varying q^* values). The extended internal-flow hydraulic model is therefore applied to predict the interface heights of maximal exchange flows generated across the sill, based on the two control point ($G^2 = 1$) solutions, for the range of parametric conditions tested. For the dimensionless sill depth $h_s^* = 0.532$, Fig. 14a presents three different two-layer hydraulic model solutions: (i) idealised, inviscid maximal flow case (i.e. $\Delta E^* = 0.0$, $m = 0$); (ii) viscid maximal flow case (i.e. $\Delta E^* = 0.1$, $m = 0$); and (iii) viscid maximal flow case with saline mass transfer (i.e. $\Delta E^* = 0.1$, $m = 0.75$), over the range of

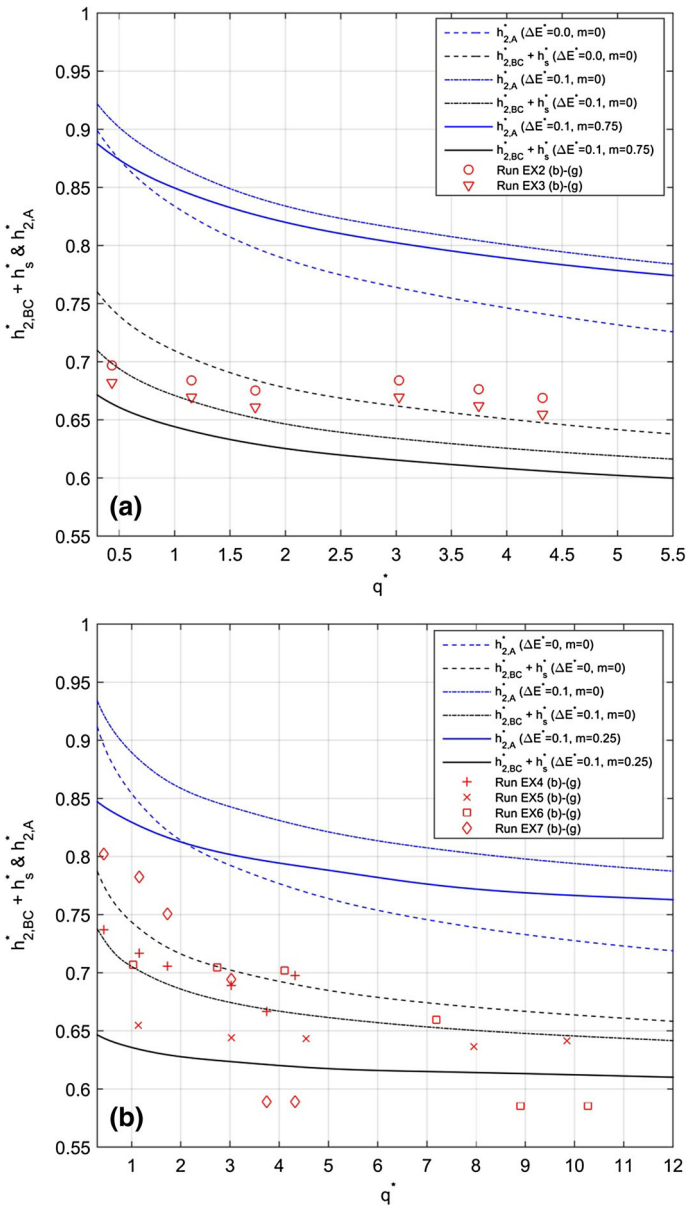


Fig. 14 Internal-flow hydraulic model predictions of normalised interface elevations $h_{2,A}^*$ and $(h_{2,BC}^* + h_s^*)$ at sections A and sill section BC, respectively (Fig. 1) plotted versus the fresh-saline flux ratio q^* for idealised ($\Delta E^* = 0, m = 0$); viscid ($\Delta E^* = 0.1, m = 0$); and viscid with mass transfer ($\Delta E^* = 0.1, m > 0$) maximal exchange flow solutions presented for sill submergence depth h_s^* of **a** 0.532 and **b** 0.588. Corresponding experimental data from measured and spatially-averaged (i.e. along the sill) $u = 0$ interface elevations ($h_{2,BC}^* + h_s^*$) are shown for comparison purposes

fresh-saline volume flux ratios ($q^* = 0.43 - 4.32$). Specifically, this figure plots the predicted non-dimensional interface heights at the two control ($G^2 = 1$) sections A and BC [i.e. $h_{2,A}^*$ and $(h_{2,BC}^* + h_s^*)$, respectively] versus q^* . The normalised $u = 0$ interface

elevations ($h_{2,BC}^* + h_s^*$) for runs EX2 and EX3, spatially-averaged across the horizontal sill crest ($-1.0 \leq x/l_s \leq 0$), are also plotted in Fig. 14a for comparison. In this context, Fig. 14a shows firstly that the idealised, inviscid model ($\Delta E^* = 0.0$, $m = 0$) solution does not agree well with measured sill-averaged interface elevations, with EX2 and EX3 data lying outside the $h_{2,A}^*$ and ($h_{2,BC}^* + h_s^*$) prediction curves (i.e. blue and black dashed lines). For the viscid model ($\Delta E^* = 0.1$, $m = 0$) solution, while agreement with the experimental data is improved, a couple of data points remain outside of the $h_{2,A}^*$ and ($h_{2,BC}^* + h_s^*$) solution curves (i.e. blue and black dot-dashed lines). Finally, by adding a finite mass transfer term m into the viscid model ($\Delta E^* = 0.1$, $m = 0.75$), all experimental data points for $u = 0$ heights are shown to lie within the $h_{2,A}^*$ and ($h_{2,BC}^* + h_s^*$) solution curves (i.e. solid blue and black lines).

The extended internal-flow hydraulic model is similarly applied to predict the non-dimensional interface heights $h_{2,A}^*$ and ($h_{2,BC}^* + h_s^*$) at the dimensionless sill depth $h_s^* = 0.588$, with the three distinct model solutions (i) inviscid, (ii) viscid, and (iii) viscid with mass transfer, plotted in Fig. 14b over the range of q^* values (0.3–10.3) shown. As with Fig. 14a, some of the measured $u = 0$ interface elevation data plotted in Fig. 14b (i.e. runs EX4–EX7) lies outside the $h_{2,A}^*$ and ($h_{2,BC}^* + h_s^*$) solution curves from both the inviscid ($\Delta E^* = 0.0$, $m = 0$) and viscid ($\Delta E^* = 0.1$, $m = 0$) model predictions, while all measured interface data across the sill lies within the $h_{2,A}^*$ and ($h_{2,BC}^* + h_s^*$) solution curves of the viscid with mass transfer ($\Delta E^* = 0.1$, $m = 0.25$) model prediction. It should be noted that the four data points that remain outside these solution curves correspond to the four runs [i.e. EX6(f),(g) and EX7(f),(g)] where dynamic blocking of the saline layer occurred across the sill, and where ($h_{2,BC}^* + h_s^*$) $\rightarrow h_s^*$ (i.e. $h_{2,BC}^* \rightarrow 0$) by definition.

The comparisons in Fig. 14a, b between the extended two-layer hydraulic model predictions of interface elevations and the corresponding experimental data highlight the importance of specifying appropriate energy loss ΔE^* and mass transfer m coefficients to accurately predict interface elevations for bi-directional stratified flows generated across the sill. In Fig. 14a, setting $m = 0.75$ clearly represents a 25% reduction in the lower saline layer volume flux between the two control ($G^2 = 1$) points, while the lower $m = 0.25$ value specified in Fig. 14b represents a 75% reduction in saline volume flux between these control points. This also appears to be largely consistent with the maximum reduction in local saline volume flux across the sill of 86%, calculated from synoptic PIV velocity fields (see Sect. 5.2).

In general, the extended two-layer hydraulic model developed is shown to provide reasonable predictions of the measured interface elevations across the sill over the range of bi-directional stratified flows generated for different q^* values. For both dimensionless sill submergence depths, $h_s^* = 0.532$ and 0.588 , it is shown that careful selection of the internal-flow head loss ΔE^* and saline mass transfer m coefficients, which are mutually independent, is clearly crucial to predicting the experimentally determined interfaces.

7 Concluding remarks

The current study has investigated the development of exchange flows across a submerged sill obstruction through a large-scale experimental study and complementary theoretical analysis using an extended two-layer internal-flow hydraulic modelling approach. The experiments focused on obtaining detailed synoptic velocity fields of these exchange flows from PIV measurements across the sill, as well as corresponding density profiles at specific sill locations using micro-conductivity probes. The synoptic velocity fields typically

indicated that the lower saline intrusion layer reduced in overall thickness h_2 as the net-barotropic flow component in the upper fresh water layer increased (i.e. fresh-saline flux ratio q^* increased). In the majority of runs, however, this dominant upper freshwater flow (i.e. $q^* > 1$) was insufficient to block the saline intrusion across the sill completely. This dynamic blocking only occurred in runs EX6 and EX7 under exchange flow conditions with the strongest net-barotropic component in the upper fresh layer (i.e. highest q^* values), and for the parametric combination of reduced sill submergence depth h_b and density difference $\Delta\rho$ between the fresh and saline waters. Indeed, the experiments demonstrated that the magnitude of a densimetric Froude number based on the upper fresh water flux q_1 and the sill submergence depth h_b was required to exceed 0.125 for dynamic blockage of the saline intrusion layer, irrespective of the magnitude of the source fresh-saline volume flux ratio q^* . For exchange flows with increasing net-barotropic components in the upper fresh layer, the presence of sharp slope discontinuities in the trapezoidal sill and sill-basin transitions was also expected to influence interfacial mixing, entrainment and the eventual blockage of the saline intrusions. However, no direct experimental evidence was observed to suggest that the sill and basin geometry, apart from the submergence depth h_b , played a significant role in the dynamic blocking of the saline intrusion. As such, it is anticipated that the parametric conditions required for saline layer blockage across the experimental sill (i.e. $q_1/(g'_0 h_b^3) > \sim 0.125$, Fig. 6) may also be applicable to real estuarine conditions with dominant net-barotropic flows in the upper fresh water layer.

Local fresh \hat{Q}_1 and saline \hat{Q}_2 water fluxes were calculated at both ends of the horizontal sill crest to examine the mass transfer between the counter-flowing layers. At the marine basin M end of the sill (i.e. $x/l_s = -1.0$), the local flux ratio \hat{Q}_1/\hat{Q}_2 was found to vary over a similar range to the source fresh-saline volume flux ratio q^* , while close to the impoundment I end of the sill (i.e. $x/l_s = -0.15$), this local flux ratio \hat{Q}_1/\hat{Q}_2 increased significantly (Fig. 8). Importantly, this finding was indicative of a significant reduction in the lower layer flux \hat{Q}_2 in the direction of the saline intrusion across the sill, which also tended to increase with increasing net-barotropic flow in the upper fresh water layer (i.e. higher q^* values). This represented significant mass exchanges of up to 86% from the lower saline layer to the upper fresh water layer, driven by interfacial entrainment under increasingly dominant upper freshwater flows (i.e. $q^* \gg 1$). It was therefore important to represent this mass transfer coefficient as an internal-flow process in the extended two-layer hydraulic modelling approach used to predict the dynamic behaviour of restricted exchange flows with net-barotropic components.

The levels of interfacial mixing in the bi-directional stratified flows generated across the sill were indicated by the significant instabilities observed in the recorded density profiles (Fig. 9), especially at the impoundment I end of the sill (i.e. $x/l_s = 0$). A quantitative measure of the normalised mixing layer thickness δ/h_b was determined from the vertical separation of the $\rho' = 0.2$ and 0.8 isopycnals in vertically-sorted density profiles across the sill (Fig. 10). This mixing thickness was shown (Fig. 11) to increase with the modified densimetric Froude number $q_1^2/(g'_0 h_b^3)(1/q^*) = q_1 q_2/(g'_0 h_b^3)$, indicating that for a prescribed saline volume flux q_2 , increasing the fresh water volume flux q_1 and/or reducing g'_0 or h_b tends to result in increased interfacial mixing. Corresponding estimates of the Thorpe overturning length scales L_T (Fig. 12) were also shown to increase monotonically as q^* increases, approaching 40–50% of the overall sill submergence depth h_b in some cases, especially close to basin I (i.e. $x/l_s = 0$). Clearly, these large-scale instabilities may be indicative of large, shear-induced, Kelvin–Helmholtz-type billows generated on the density interface at the leading edge of the sill crest under exchange flows with strong net-

barotropic components in the upper layer. However, the relatively long time scale of the density profiling measurements meant that the estimated L_T values were more likely to be indicative of ensemble-averaged mixing characteristics rather than the identification of individual instabilities. In this regard, the nature of the interfacial instabilities generated across the sill, as well as the mixing and entrainment mechanisms leading to blockage of the saline intrusion layer, may have been better identified using a two-phase PIV/PLIF system.

Estimates of the composite Froude number G^2 were also obtained from the synoptic PIV velocity fields and density profile measurements across the sill. This indicated that the bi-directional stratified flow conditions generated across the sill remained subcritical (i.e. $G^2 < 1$) in all runs and for all q^* values, although with G values typically increasing towards the impoundment I end of the sill (i.e. $x/l_s \rightarrow 0$). It is noted here that under the idealised, inviscid, two-layer hydraulic modelling of maximal exchange flows with a net-barotropic component in the upper layer, a second internal control point (i.e. $G^2 = 1$) would be expected to form across the sill region of uniform depth and width (i.e. between sections B and C , Fig. 1). However, the fact that the exchange flow conditions across the sill remained subcritical (i.e. $G^2 < 1$) throughout suggests that this second internal hydraulic control point ($G^2 = 1$) is displaced to a location in the freshwater impoundment I .

An extended internal-flow hydraulic model has been developed to predict interface elevations at the two control sections A and at a sill section BC , assuming that maximal exchange flow conditions are generated across the sill, which were compared with spatially-averaged $u = 0$ velocity interface elevations measured across the sill crest. Predictions from the extended two-layer hydraulic model were obtained for the idealised, inviscid flow case (i.e. $\Delta E^* = 0$, $m = 0$), the viscous flow case (i.e. $\Delta E^* = 0.1$, $m = 0$), and the viscous flow case with finite saline mass transfer to the upper fresh water layer (i.e. $\Delta E^* = 0.1$, $0 < m < 1$). In general, reasonable agreement was observed between the predicted interface elevations $h_{2,A}^*$ and $(h_{2,BC}^* + h_s^*)$ and measured elevations across the sill, when appropriate values of the internal energy loss $\Delta E^* (= 0.1)$ and saline mass transfer m ($= 0.75$ and 0.25) coefficients were specified in the extended two-layer hydraulic model. In particular, the specification of $m = 0.25$, corresponding to a 75% mass transfer of saline flux into the upper fresh water layer, appears to be in general accord with the calculated maximum saline volume flux \hat{Q}_2 reduction of 86% across the sill, where a bi-directional stratified flow is still present. Furthermore, it is also noted that for the experimental runs in which the saline intrusion layer is dynamically blocked, the corresponding saline mass transfer coefficient $m = 0$ by definition, representing full entrainment of the saline layer into the upper fresh layer. It can therefore be concluded that the combined effect of bottom friction and interfacial entrainment is important in determining the behaviour of bi-directional stratified flows generated across the submerged trapezoidal sill obstruction, and defining the conditions under which dynamic blocking of the saline intrusion occurs. More general application of the extended two-layer model developed in this paper to a wider range of restricted exchange flow configurations would require a detailed sensitivity analysis into its predictive capabilities over different sill and channel constriction geometries and over specified ranges of ΔE^* and m values; both of which are beyond the scope of the current paper.

Acknowledgements The authors would like to thank Prof. Jarle Berntsen, Dr. Øyvind Thiem, Dr. Madis-Jaak Lilover, Mr. Jonathan Kean and Ms. Monika Kollo for their invaluable help in the experimental study. They would also like to thank the technical staff at Laboratoire des Écoulements Géophysiques et Industriels (LEGI), Grenoble, for their support during, and subsequent to, the access period at the Coriolis Rotating

Basin Facility. The work has been supported by European Community's Seventh Framework Programme through the grant to the budget of the Integrating Activity HYDRALAB IV within the Transnational Access Activities, Contract No. 261520. The ADV instrument used in the study was provided by TUT (IUT 19–17). The authors are also grateful to the three anonymous reviewers whose extensive comments have led to significant improvements in the manuscript.

Open Access This article is distributed under the terms of the Creative Commons Attribution 4.0 International License (<http://creativecommons.org/licenses/by/4.0/>), which permits unrestricted use, distribution, and reproduction in any medium, provided you give appropriate credit to the original author(s) and the source, provide a link to the Creative Commons license, and indicate if changes were made.

References

1. Armi L, Farmer DM (1986) Maximal two-layer exchange through a contraction with barotropic net flow. *J Fluid Mech* 164:27–51
2. Cuthbertson AJS, Davies PA, Coates MJ, Guo Y (2004) A modelling study of transient, buoyancy-driven exchange flow over a descending barrier. *Environ Fluid Mech* 4:127–155
3. Cuthbertson AJS, Laaneau J, Davies PA (2006) Buoyancy-driven two-layer exchange flows across a slowly submerging barrier. *Environ Fluid Mech* 6:133–151
4. Dalziel SB (1991) Two-layer hydraulics: a functional approach. *J Fluid Mech* 223:135–163
5. Farmer DM, Armi A (1999) Stratified flow over topography: the role of small-scale entrainment and mixing in flow establishment. *Proc R Soc Lond A* 455:3221–3258
6. Farmer DM, Armi A (2001) Stratified flow over topography: model versus observations. *Proc R Soc Lond A* 457:2827–2830
7. Fouli H, Zhu DZ (2011) Interfacial Waves in Two-layer Exchange Flows Downslope of a Bottom Sill. *J Fluid Mech* 680:194–224
8. Head MJ (1983) The use of four electrode conductivity probes for high resolution measurement of turbulent density or temperature variation in salt-stratified water flows. Ph.D. dissertation, University of California, San Diego
9. Inall M, Cottier FR, Griffiths C, Wiles P (2004) Sill dynamics and energy transformation in a jet fjord. *Ocean Dyn* 54:307–314
10. Inall M, Rippeth TP, Griffiths C, Wiles P (2005) Evolution and distribution of TKE production and dissipation within stratified flow over topography. *Geophys Res Lett* 32:L08607
11. Johnson HL, Garrett C (2004) Effects of noise on thorpe scales and run lengths. *J Phys Oceanogr* 34:2359–2372
12. Kõuts T, Laaneau J (2001) Variability of currents in Bays of Tagalaht and Uudepanga. *Proc Estonian Acad Sci* 7(2):126–140
13. Laaneau J, Lips U (2003) Observed thermohaline fields and low-frequency currents in the Narva Bay. *Proc Estonian Acad Sci Eng* 9(2):99–106
14. Laaneau J, Koppel T, Soomere T, Davies PA (2007) Joint influence of river stream, water level and wind waves on the height of sand bar in a river mouth. *Nord Hydrol* 38(3):287–302
15. Laaneau J, Davies PA (2007) Hydraulic control of two-layer flow in “quadratic”-type channels. *J Hydraul Res* 45(1):3–12
16. Laaneau J, Vassiljev A, Davies PA (2011) Hydraulic modelling of stratified bi-directional flow in a river mouth. *Proc Inst Civ Eng Eng Comput Mech* 164(4):207–216
17. Laaneau J, Cuthbertson AJS, Davies PA (2014) Dynamics of dense gravity currents and mixing in an up-sloping and converging vee-shaped channel. *J Hydraul Res* 52(1):67–80
18. Lilover MJ, Lips U, Laaneau J, Liljebldh B (1998) Flow regime in the Irbe Strait. *Aquat Sci* 60(3):253–265
19. Lilover MJ, Stips A (2008) The variability of parameters controlling the cyanobacteria bloom biomass in the Baltic Sea. *J Mar Syst* 74:S108–S115
20. Negretti ME, Zhu DZ, Jirka GH (2007) Barotropically induced interfacial waves in two-layer exchange flows over a sill. *J Fluid Mech* 592:135–154
21. Negretti ME, Zhu DZ, Jirka GH (2008) The effect of bottom roughness in two-layer flows down a slope. *Dyn Atmos Oceans* 45(1–2):46–68
22. Sargent FE, Jirka GH (1988) Experiments on saline wedge. *J Hydraul Eng ASCE* 113(10):1307–1323
23. Thorpe SA (1977) Turbulence and mixing in a Scottish loch. *Philos Trans R Soc Lond* 286A:125–181
24. Zhu DZ, Lawrence DA (2000) Hydraulics of exchange flows. *J Hydraul Eng ASCE* 126:921–928